Improving Imaging Techniques and Resolution in Neutron Radiography

BY

NICHOLAS P BORGES

ABSTRACT OF A DISSERTATION

SUBMITTED TO THE FACULTY OF THE

DEPARTMENT OF PHYSICS

IN PARTIAL FULFILLMENT OF THE REQUIREMENTS

FOR THE DEGREE OF

DOCTOR OF PHILOSOPHY

PHYSICS

WORCESTER POLYTECHNIC INSTITUTE

2020

Thesis Supervisor: David C Medich, Ph.D.

Associate Professor, Department of Physics

Abstract

Hydrogenous samples, such as biological tissues, analyzed in a neutron radiography geometry display reduced image contrast and resolution due to excessive image contributions from scattered neutrons produced from the high neutron-scatter cross section with hydrogen. Because of this, neutrons presently are not used for thick-tissue(>2.5cm) or in-vivo imaging. Two methods of neutron scatter rejection and event centroiding, were employed to enhance the quality of biological neutron imaging by reducing image blurring noise caused by hydrogen and increasing the contrast ratio of the detector. By employing the techniques used herein, event centroiding can increase the natural resolution of the detector by a factor of two without energy dependence and as much as 4 times with energy bins. Scatter rejection can increase the contrast resolution by 7%-10% of an imaging standard and can resolve a 160 μm image through 6mm of acrylic.

Acknowledgements

First and foremost, I would like to thank my dissertation advisor, Professor David C Medich, for his guidance and support throughout my Ph.D. career. He was always willing to go above and beyond to help me achieve any goals I have set.

I would also like to thank Dr. Sven Vogel and Dr. Adrian Losko for their mentoring in my studies at Los Alamos National Lab and training me in the world of neutron radiography and tomography.

The graduate students (both past and present) that make up the radiation group at Worcester Polytechnic Institute were vital in providing me with friendship during these long years. They were pivotal in helping me through those frustrating times when equipment and software wouldn't work.

I would like to thank my family without whom I would never have made it this far.

Lastly, I would like to thank my lovely wife, Jen. She has been there for me during the extremely long trips away from home at different national labs and has been a source of inspiration.

This research was sponsored through the NRC HQ-14-G-0053, NRC HQ-14-G-0038, and the Department of Energy / Sandia National Laboratories #1679802

Contents

List of Figures

Introduction

The use of x-rays and gamma emitting radioisotopes have been utilized in the medical field since their conception, but one type of radiation has been neglected for any type of medical imaging. Neutron imaging suffers from poor image quality due to hydrogen scattering and accessibility of highly collimated beams outside of national labs and nuclear reactors. The ratio of scatter vs absorption of neutrons is over a hundred times higher for thermal neutrons and about 50 times higher for epithermal. If the scattered neutrons is rejected or converted to absorbed neutrons the ratio of information gained to the radiation damage to cells would be higher than that of x-rays.[0]

1.1 History of Medical Imaging

The introduction of X-rays in 1895 by Wilhelm Conrad Röntgen sparked a new curiosity for applications in industry and the medical world. Röntgen demonstrated that the Hittorf-Crookes tube will fluoresce after energizing a cathode ray tube. The fluorescence would continue even when heavy black paper and other solid material was placed in between the cathode ray tube and the Hittorf-Crookes tube.

He would go on and demonstrate that these rays could create an image of lead weights inside a box[1]. These invisible short-wavelength electromagnetic rays were able to penetrate hydrogenous materials with ease and completely stopped by bone and metal as shown in figure 1. Röntgen did not know what to call this new form of ray so he named it experiment "X" as in the unknown ray, thus led to the term X-ray. Röntgen won the Nobel Prize for his discovery of the X-rays in 1901.[4]

Figure 1: X-ray image of Wilhelm Conrad Röntgen's wife, Bertha's, hand with a ring on

In 1900, X-ray machines were being produced for hospital use and became pivotal in diagnosing foreign bodies or fractured bones within patients. By 1925, 25% of all patients admitted to a Pennsylvania hospital were undergoing some form of X-ray imaging procedure.[3] The simplicity of taking static X-rays were available in smaller hospitals, but over time researchers started experiment with taking stacked images to produce an X-ray movie.

Fluoroscopy, moving X-ray images, were invented within 20 years of the first patient to be X-rayed in a hospital. The new technique was advantageous for detecting cancers of the esophagus, stomach, and bowel when patients would swallow radio-opaque barium in a drink.[3]

While techniques and imaging detectors were being optimized for decreasing dose to patients and creating higher quality images, the next biggest imaging breakthrough wasn't until 1967. Around 1940, X-ray tomography is described as multiple x-ray images around a point of interest to recreate anatomical slices throughout the object. This was to solve the issue when some tissues were obscured behind objects. The idea for x-ray tomography was scientifically possible but the electronic technology hasn't developed quickly enough.

Godfrey Hounsfield described a machine capable to handle Computed Axial Tomography (CAT or CT) called the EMI-Scanner. The first hospital unit can be seen in Figure 2, that was install on 1971 in England. Hounsfield's discovery led to his Nobel Prize awarded in 1979.

Figure 2: The first commercially available EMI-Scanner in1971.[4]

This new technology allowed for 3d images of patients brains and would help physicians diagnose brain abnormalities.

Concurrently with the progress of CT scanner developments, a process that does not use radioactive isotopes was conceived. Magnetic Resonance Imaging (MRI) utilizes strong electromagnets to alter spin states of atoms. The relaxation of atoms that are altered can be detected while they give of their excess energy and images can be processed. The advantages of MRIs are that the images do not provide images on structural parts of the body (bones and joints), but allows functional imaging. Functional imaging consists of movement of muscles, reactions in the brain, and heart functions.

The MRI was invented by Paul C. Lauterbur using the principles of Nuclear Magnetic Resonance and applied that to create an image in 1980. Awarding hin the Nobel Prize in 2003.[5] Raymond Damadian would then go and build the first MRI machine to image a living person. The scan took 5 hours to complete and the lab assistant that was imaged need to lay still to not affect the image quality. There is controversy behind Damadian not receiving the Nobel Prize with Lauterbur due to his contributions of imaging a living person.

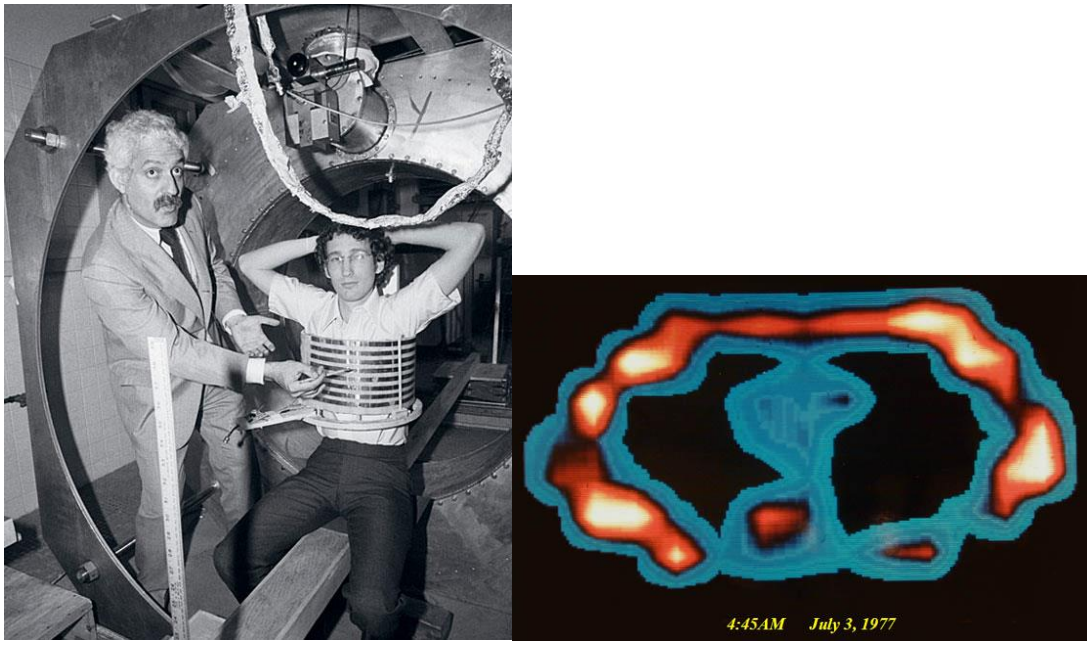

Figure 3: Raymond Damadian pointing to Larry Minkoff inside the receiver coil and the resultant interpolated image of the Minkoff scan resulting in the first ever MRI scan of a live human being[6]

Over time, image quality of all of these modalities increased along with decreasing imaging times. Advancement in technologies would allow for imaging techniques to no longer need to film development and computers will handle all of the calculations for tomography. In the 120 years since the first X-ray, new techniques and modalities are still being refined for therapeutic and diagnostic purposes in hospitals.

1.2 Principles of Imaging

The creation of an image depends on the contrast between a high absorption material and a low absorption material. The intensity of a narrow beam if xrays/gammas/neutrons through a material is dependent on thickness and a material linear attenuation coefficient(as seen in the following equation).

$$I_x = I_o e^{-\mu x}$$

Where: I_x = the intensity of photons transmitted across some distance x

I_0 = the initial intensity of photons

m = the linear attenuation coefficient

x = distance traveled

The differences in the transmission of the beam through different materials will give different intensities which can be quantified visually. The linear attenuation coefficient is different for x-rays and neutrons.

X-rays interact with atomic electrons as the atomic number increases, the probability that the x-ray will interact with the material increase as well. This will create a contrast between the two materials that can be quantified. There are two methods that x-ray interact with materials. The first is the photoelectric effect, where a photon uses up all of its energy to eject an electron from an atom; while the electron will move around and ionize neighboring atoms. The second major effect is Compton scatter, where a photon hits an atom and ionizes an electron but does not use up all of its energy. The photon then scatters in a different direction with a bit less energy. This scattered photon, if it reaches the detector, degrades image quality. Atoms that have a smaller electron densities, like hydrogen and oxygen, will not interact readily with the x-rays, this results in tissues that have different hydrogen content will not be easily quantified. The difference between tissue and bone for example is able to be easily resolved, because the

x-ray interaction with calcium in the bone is considerably higher than that of hydrogen in the tissue.

Neutrons interact only with the nucleus and deviate from their trajectory via scattering directly off the nuclei or getting absorbed. Neutrons interacting directly with nuclei allows different interaction rates to different isotopes of the same elenment. Neutrons interact readily with hydrogen, and nitrogen (and to a lesser extent carbon and oxygen). Therefore, neutrons are very sensitive to local changes in a tissue's H, C, O, N content. This will not only give functional information about different tissues, but also give information on structural objects in the body. Whereas x-rays cannot resolve different tissue types.

With any type of imaging there is certain artifacts that degrade image quality. One of the significant contributors to image degradation is scatter. An x-ray or neutron that is scattered or deflected off trajectory between the object and imaging plate creates a blurred image instead of a highly defined line between the contrasting mediums. One solution to correct the blurring due to scatter is to stop the deflected particles from interacting with the imaging plate. In x-ray imaging, this type of device is called a bucky grid, it has leaded slots that only allow x-rays that are coming straight through the patient into the detector. Removing the scatter will decrease the incoming particles to the detector, thus increases imaging time but the result is a high spatial resolution image. The spatial resolution is the ability to resolve between two objects.

1.3 Detection Modalities

Structural Imaging

Current technologies for X-ray images allow imaging and fluoroscopies that are individual to every single patient. There are specialized machines for bone density imaging, mammographies, whole body and extremity CT machines, and the list continues on. Typically radiographs (2d images) or tomographies (3d reconstructions) allows a physician to visualize anatomical structures smaller than 0.3 mm and offers good contrast between different material types, like bone and healthy tissue but cannot easily distinguish between different tissues without the aid of a contrasting agent.

Comparing the resolution between structural imaging techniques depends on the detector size and the magnification of the beam, but in general the resolution given for structural imaging in hospital settings is as follows;

CT scans can resolve an object that is 0.5mm[25]

General radiography can resolve an object that is 0.08mm[26]

Mammography can resolve an object around 0.03-0.05mm[26]

Functional Imaging

There are two main modalities for obtaining functional images in a patient. Injecting a patient with radioactive material and detecting the radiation on the outside of the patient or injecting a contrast agent that is opaque to traditional radiation imaging or magnetic imaging.

Nuclear Medicine

Ingesting or injecting a radionuclide into the body provides a unique look into how a drug interacts and where the drug congregates. The typical isotopes used in Positron-Emission Tomography (PET) or Single Photon Emission Computed Tomography (SPECT) are 100% beta+ emitters and have extremely short radioactive half-lives and biological half-lives (less than thirty minutes). The resolution for a typical PET or SPECT image is 4-10mm and 4-15mm respectively.[25]

These imaging types may have poor spatial resolution characteristics, but allows functional information for assessing tissue metabolic activity, diagnosing malignant cancer sites or observing physiology. The poor resolution usually means that the images need to be enhanced by another imaging method. PET machines are often combined with CT machines to provide a higher resolution backbone to the blurrier functional image.

Magnetic Resonance Imaging

Magnetic Resonance Imaging uses non-radioactive contrast agents to locate areas of interest where a drug can congregate in the body. This modality uses a pulsed magnetic field to polarize hydrogen atoms in a subject. Between pulses, the hydrogen atom relaxes and the MRI is able to take that signal and create a 3 dimensional image. This can give both functional and anatomical/structural imaging but suffers in the ability to resolve objects. The resolution for functional MRI is 1-2mm.[25] Other disadvantages of MR scanning is the acquisition time ranges between 45 minutes to over an hour, where the patient must remain still throughout the procedure. Also, no ferromagnetic material can enter the facilities due to the possibility that the magnet within the scanner can pull the object into the bore.

1.3 Neutron imaging

Neutrons have the unique property that they interact directly with the atomic nucleus, unlike photons which interact with atomic electrons. This means that neutron radiography can benefit by having different cross sections for isotopes of the same element and can produce different contrast images based on isotope makeup of the sample. Neutron are categorized by their energy in electron volts (eV) or temperature. Cold neutrons are neutrons with energies from 0 eV to 0.025 eV. Thermal neutrons have energies at 0.025 eV to 1 eV. Epithermal neutrons range between 1eV-1keV. Lastly, fast neutrons are 1 keV and above.[27] These different energies of neutrons have different cross sections for the same elements, As seen in Figure 4, an energy dependent neutron beam and distinguish between enrichment levels of uranium.

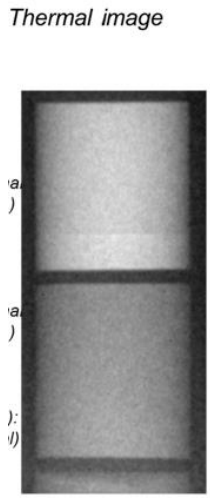

Figure 4: Neutron computed tomography (CT) of UN/U_3Si_5 and U_3Si_5 fuel pellets with different enrichment levels of uranium. The thermal neutron radiography can distinguish between the 8.84% and 0.2% enrichment of U238 in the fuel pellet.[7]

Neutron radiography has very high spatial resolution and efficiency in certain samples. Detectors setups and samples can even achieve up to 4.8μm.[28] Neutrons readily scatters in biological materials when interacting with the hydrogenous tissues. This

scatter degrades the spatial and contrast resolution of the image and has been a major source of discouragement against imaging biological materials.

Materials and Methods

2.1 Neutron Sources

2.1.1 Adelphi Tech Generator

The Adelphi Technology Neutron Generator (DD-110m seen in figure 5) uses the basic fusion of deuterium atoms (D + D) that results in the formation of a He-3 ion and a neutron with a kinetic energy of approximately 2.5 MeV. The neutrons are then moderates to thermal range (0.025 eV). Neutrons produced from the fusion reaction are emitted isotropically (uniformly in all directions when unshielded). In all cases, the associated He nuclei (alpha particles) are emitted in the opposite direction of the neutron. The Uniformity of the neutron distribution was computationally calculated using MCNP 6(figure 6).

Figure 5: Picture of the WPI radiation physics lab unpacking the new Adelphi DD110M neutron generator.

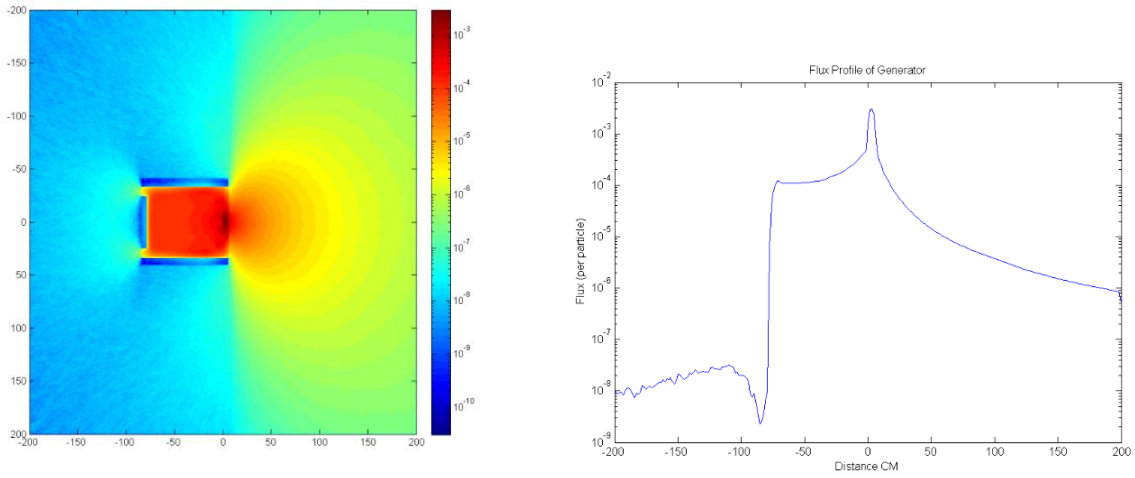

Figure 6: MCNP 6 computer simulation of the flux of thermal neutrons out the front of the generator. Resulting thermal flux of neutrons is $1x10^7$ neutrons/cm^2/second at beam face

2.1.2 University of Massachusetts Lowell Research Reactor

The UMLRR is a 1MW pool-type nuclear research facility; a design in which the Low Enriched Uranium core is cooled by direct submersion within a 35-foot-deep pool. The reactor produces a spectrum of neutron energies moderated to thermal neutrons for radio-activation and neutron radiography applications.[8]

Figure 7: Cadmium lined evacuation chamber with decrease pressure for beam collimation.

The nuclear reactor has multiple different rooms for irradiations but the thermal neutron port has a collimated beam and is ideal for neutron imaging. The ratio of faster neutrons to thermal neutrons creates some unwanted interactions with the detector

since we are only interested in the thermal range. Figure 8 shows the purity of the thermal neutron beam.

Broad Group Fluxes (n/cm2-sec)

Fast Flux (>0.1MeV)	3.44 E11
Epithermal Flux	4.65 E11
Thermal Flux	3.17 E12
Total Neutron Flux	3.98 E12
Total Gamma Flux	9.97 E12

Figure 8: Composition of the thermal imaging beamline.

2.1.3 Los Alamos National Lab (LANSCE Facility)

Imaging measurements described in this report were performed using Flight Path 5 (FP5) at the Lujan Neutron Scattering Center (for a description see M. Mocko et al.). The spallation neutron pulses are created by 270 ns long 800 MeV H+ pulses impinging on a tungsten target. The neutrons are then moderated using liquid water at room temperature and collimated using 2.5 to 5 cm thick steel and polyethylene disks with round holes of diameters increasing from 2 cm to 5 cm from 4.5 m to 6 m distance from the moderator. At 6 m from the moderator, additional 20 cm of steel and poly disks with round holes of 0.5 cm are used to further collimate the beam for high resolution measurements (Figure). The resulting spectrum for neutrons at the Lujan center is shown in 10. It provides a thermal neutron flux of ~2.4 × 10^7 n·cm^{-2}·s^{-1} at ~8.8 m from the moderator with a peak at 25 meV.[9,10]

Lujan Center's ASTERIX beamline (1FP-11) modifies the beam to allow for a thermal/cold neutron beam only. The beamline uses a liquid hydrogen moderator providing cold neutrons that are especially suited for performing phase-contrast imaging. Phase contrast imaging provides contrast enhancement of edges, voids and other defects in materials that otherwise have contrast too poor for imaging.[7] A 6 cm × 6 cm neutron guide transports the cold neutrons 15.1 m from the moderator to a variable aperture which can be opened to maximize flux for cold neutron radiography or reduced to provide a more collimated beam for neutron phase contrast imaging. [9,10]

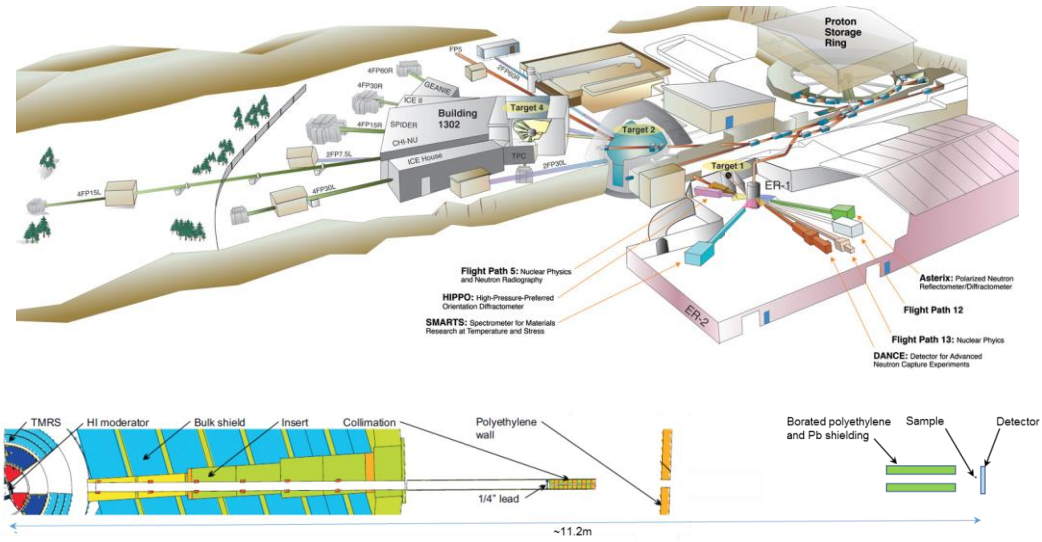

Figure 9: Flight Path 5 Schematic located at Target 1 within the ER-1 facility. Note that the polyethylene walls and the borated polyethylene and Pb shielding were not used for the measurements reported here.

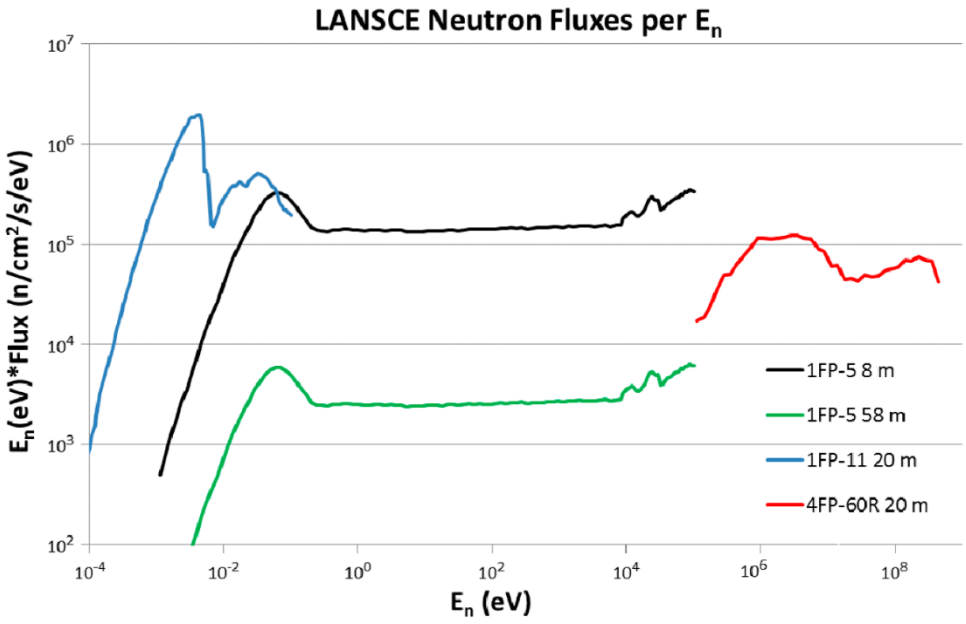

Figure 10: The total neutron energy spectra produced by the Lujan Center. The spectra were calculated with the maximum proton beam currents of 125 μa for the Lujan Center[10]. Unmoderated Target 2 allows 4FP-60R to be used for fast neutron imaging. FP-5 58m is an extension from the FP-5 beamline and is used for material analysis.

2.2. Neutron Detection and Experimental Setup

There is a many different detector types for neutron radiography and tomography (as seen in figure 11). The main principle is similar for all types of detection, being to slow down the neutron and interact with it to create light. A scintillator screen or a multi-channel plate convert the neutron to either photons or electrons that can then be quantified by a digital detector.

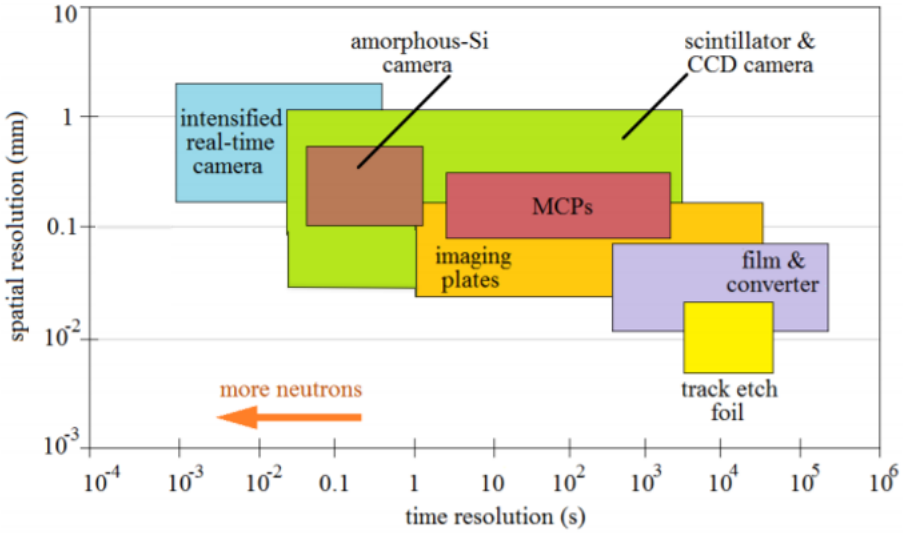

Figure 11: Graph depicting spatial and temporal resolution for a majority of neutron radiography setups.[11]

2.2.1 Affordable Neutron Radiography with CCD

A typical neutron radiography setup using a CCD camera using a scintillator to convert the neutron beam to a light source. The light source is then picked up by CCD chip in the camera. The scintillator is a crystalline material made up of Gd_2O_2S:Tb and mixed with 20%^{6}LiF. This crystal utilizies the large neutron cross section of Gd to absorb the neutrons and create a secondary radiation interaction. The secondary reaction creates photon luminescence due to the Tb and LiF within the crystal.[12]

The combined system with CCD camera, andor ikon xl camera, and scintillator setup can range upwards of $50,000 for high resolution and low noise systems. More affordable systems have comparable resolutions but slightly increased noise. An

astronomy CCD camera, ZWO ASI183MM, with a LiF scintillator costs around $2,500 and can achieve sub 60 um resolution.

The gadolinium oxide scintillator has >90% thermal neutron conversion efficiency and with a low noise peltier cooled CCD that is able to pick up minute levels of light, creates an effective imaging system.[13]

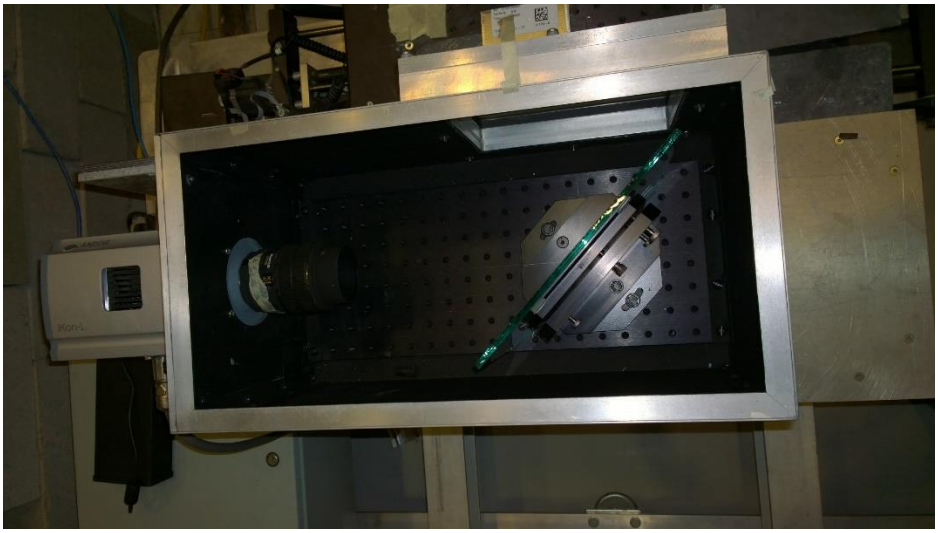

Figure 12: Typical CCD radiograph detector setup including a 90 degree mirror to move Andor ikon CCD camera out of neutron beam.

2.2.2 The Time-of-Flight (Medipix) Detector

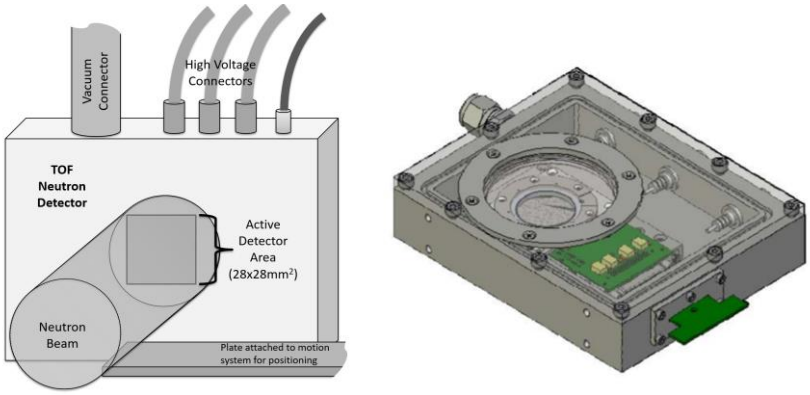

Figure 13: Detector schematic.

The pixilated neutron Time of Flight (TOF) imaging detector used at FP5 is custom-designed and manufactured and shown in Figure 13. It consists of a Gd/B doped microchannel plate (MCP) and MediPix read-out chip[14,15]. The Medipix MCP detector at the LANSCE facility allows for single neutron event detection due to the high efficiency (50–70% for thermal neutrons)[16] and has a 100 kHz frame rate in single particle mode. Single particle mode have better noise supression as compared to charge-integration mode that CCD detectors use. The Medipix detector views a MCP doped with boron and gadolinium and coupled with another stack of MCPs to provide amplification. The size of the channels for the doped MCPs are 8 μm and the amplifiers have 10 μm channels. The detector sensor utilizes a complementary metal–oxide–semiconductor (CMOS) chip with four 256 × 256 arrays of pixels that are 55 μm^2 pixels. The detector is held under vacuum and provides energy resolution by the TOF method with the supply of a time zero event trigger pulse, generated by the proton pulse immediately before hitting the spallation target.

2.2.3 Event Centroiding

Event centroiding is a post processing technique, typically used in astronomy, to improve the resolution of an image[29,30]. Single event interactions on the CCD or CMOS pixels that span multiple pixels can be expanded and averaged down to a sub-pixel. This process will be utilized by the time of flight CMOS detector due to the extremely high frame rate. This allows the system to project individual frames be quick enough to have single interactions per pixel. Individual frames are then summed together to create a stacked image.

Individual neutron interactions are quantified by location and number of pixels activated. Noise within a CCD or CMOS detector can be attributed to a single pixel activation because it is unlikely that two random noise event happen in near proximity

to create clusters. A single neutron interaction is acceptable to be centroided when the number of pixels activated is between two and twenty for the time of flight detector but will vary on the size of the light pulse with a scintillation setup. Single pixel events cannot be centroided due to no extra information gained from taking the center of a point. This allows the removal of noise and the potential case of two neutrons interacting near the same pixel. The entire image is expanded by a factor of 5 in both the x and y direction which allows for the event to be centroided to a single sub-pixel. There is not enough resolution gain for a smaller multiplication factor and the imaging time would be too long for higher magnitudes.

A non-weighted center-of-mass centroiding average is applied to each event and the resulting event will fit into a single sub-pixel. The centroiding process takes the average x value and y value of the pixel is taken to create a center point of the even. There are different methods for weighted center-of-mass or other calculations to separate overlapping events, but this was not possible with the current experimental setup. The detector senses an event as either a zero or one as a value per frame. This negates any ability to create a weighting factor of sizes of events.

2.2.4 Scatter Rejection

Neutrons scatter regularly when interacting with hydrogen and contributes to image blur. To combat this increased blur from hydrogenous material there are two ways to remove scattered neutron, an anti-scatter grid ca be placed directly after the scattering material or moving the sample far enough away that the scattered neutrons will not interact with the detector. The neutron beam must be highly collimated to allow increasing the distance to remove scatter. For compact setups and with beams that are not as collimated, an anti-scatter grid will artificially create the distance to remove scatter. This allows all

neutrons that pass through the object to interact with the imaging detector and any neutrons that are scattered will be rejected when they interact with the wall.

Results

3.1 Event Centroiding

LANSCE Experiment

Centroiding has been used in astronomy applications since the 1980's[17] to achieve sub-pixel high resolution and star tracking. Converting this technique to neutron imaging is relatively new.[18.] In general, multiple pixels are activated when a neutron impinges on an imaging detector. The location of the neutron can be calculated by computing the center of mass or centroid of the activation distribution. In the case of the MediPix based pixilated neutron TOF detector used here, each 55 μm pixel is divided into 5 × 5 = 25 sub-pixels, resulting in an increase of the effective resolution to 55 μm/5 = 11 μm. One complexity with centroiding arises from the case when a double or triple interaction with multiple neutrons overlapping on one frame occurs. In that case, the center of mass cannot be distinguished and the calculation will result in a center of mass resultant from the overlapping events. However, in pulse charge mode it is possible to distinguish up to 50% overlap.[18] To avoid this occurrence for this work, the acquisition time was short while additionally negating any event that is greater than 20 pixels or less than 2 pixels, with acquisition time, minimum, and maximum pixel area being adjustable parameters. A single neutron event can be seen in Figure , with the zoomed in portion (Figure b) signifying the division and centroided location (Figure c) for one particle The highest spatial resolution achievable by this method is limited by the MCP's channel size

(11 μm) and pixel size on the detector.. Due to the cascade effect within the microchannels, neutrons absorbed at different locations within the same channel cannot be discriminated by this method.

Single particle events in integration mode do not provide a charge distribution across the activated pixels.[18] instead each activated pixel is incremented by a value of one. A simple non-intensity weighted centroiding process in normal integration mode will produce results slightly less accurate as compared to utilizing a Gaussian fit for a charged activation area in pulse mode. An acquisition time of 180 seconds allowed for an acceptable ratio of interacting neutrons and data save and processing time (360 seconds) while avoiding overlapping events. Unprocessed data is stored on the hard-drive and processed in a sequential order. Single neutron events can be observed within a single TOF frame before the 3197 individual time bins are summed together for a non-energy resolved image. The centroiding process can allow for the creation of general bins; cold neutrons (6 meV–25 meV), thermal neutrons (25 meV–960 meV), and epithermal neutrons (960 meV–242 eV) or leave the individual 3197 bins for resonance analysis. The method of event centroiding is utilized by running a python script in conjunction with the detector's native pixelman software. The python script takes a saved .fits file from pixelman and runs a secondary macro written for ImageJ that can centroid and convert the image to a tabulated text file for compressing larger data files(see appendix A). The general bin centroided method is presented and the advantages are discussed.

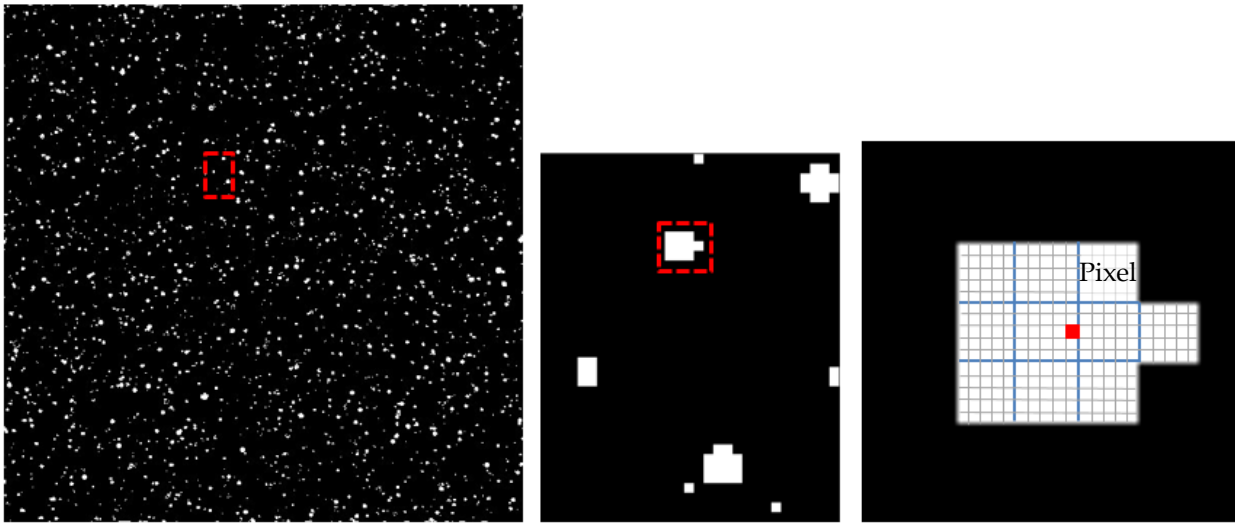

Figure 14: Neutron TOF image for the cold neutron radiograph energy region showing individual events(a). Zoomed in section of (a) marked by red dashed rectangle (b). Illustrated sub-pixel break down for a single neutron event marked by red dashed area in (c). One single 55 μm pixel is converted into a 5 × 5 subpixel array with sizes of 11 μm each. The red square indicates where the event will be centroided to a single sub pixel.

For the measurements reported here, the detector was positioned ~11.2 m from the water moderator. The test patterns to measure the resolution were produced by imaging a gadolinium (Gd) grating fabricated at the Paul Scherrer Institute, Villigen, Switzerland.[19] The resolution grating was placed as close as possible to the detector to minimize blur from beam divergence. A collimator (smallest diameter) to sample distance of about L = 5 m and smallest beam diameter of D = 0.5 cm resulted in a collimation ratio L/D of 1000. With a sample to detector distance d of ~1 cm, the geometric blur is given by d/(L/D) ≈ 10 μm (note that this blur is not the same as the spatial resolution). As an internal standard for the resonance measurements and position calibration of the detector, a 0.1 mm thick Ta sheet was placed in front of the sample (source side). To reduce background from gamma radiation emitted from the spallation

target, ~12 mm lead was also placed into the beam at the exit of the incident collimator pipe.

An open beam measurement to see the detector response with 12+ hours of acquisition time reveals that the centroiding introduces some artefacts (Figure 15). The grid in the Fourier transform, Figure 15b, of the centroided open beam image, Figure 15a, is indicative of a roughly 13 μm pattern that is consistently present throughout the entire radiograph whereas in Figure 15c, the Fourier transform of the same open beam image without centroiding, the pattern is not present. This visible pattern from centroiding is regarded as an artefact but it does not degrade the overall image. The most likely source of this artefact is produced when creating the 25 × 25 subpixels per pixel, this pattern typically happens when the centroiding program has a slight bias to the middle of the subpixels than the edges (can be seen in the zoomed region in Figure 15a). Whereas, the point in the middle of Fourier transform is an undefined point in marking the zero point and any frequency pattern is projected radially from that point. This high resolution open beam image is used for normalizing and correcting radiographs described below.

The fast Fourier transform (Figure 15b, c) converts the image into the frequency domain from the spatial domain. For example, a radiograph of 200 μm line pairs (400 μm period) on a detector with a 50 μm pixel pitch would result in a peak intensity at 8 pixels/period. If the line pairs are resolved, this would indicate a spatial-resolution of at least 200 μm.

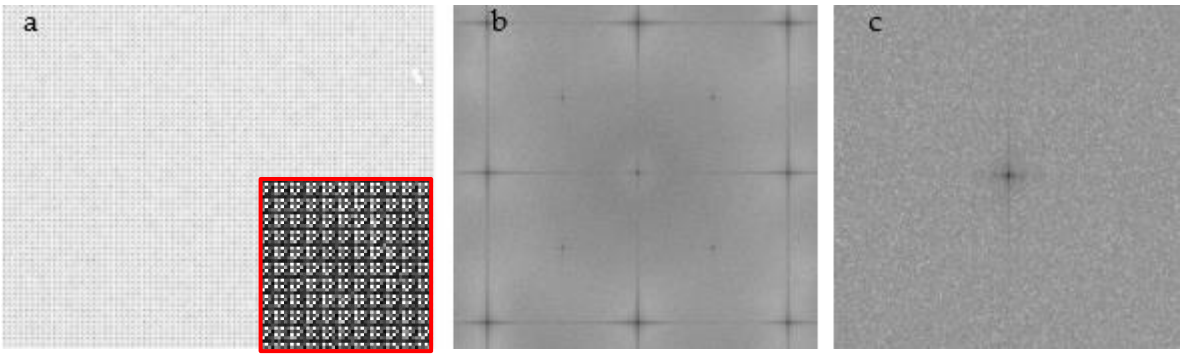

Figure 15: Centroided image with 11 μm effective pixel size for open beam radiograph. The 800% zoomed-in section to show centroiding pattern effect is in the bottom right corner (**a**). Fast Fourier transform of the centroided open beam area to demonstrate the detector characteristics which reveals some artefacts from centroiding (**b**). Fast Fourier transform of non-centroided open beam demonstrating there are no unusual artefacts in the raw data (**c**).

The Paul Scherrer Institut (PSI) resolution grating [19,20] (Figure 11) is an ideal standard for evaluating the overall resolution of an instrument setup (see reference for comparable construction of similar grating produced by PSI). The frequency of line pairs which are resolved gives a direct correlation to the overall image resolution. The grating is comprised of gadolinium regions of lines with widths of 160 μm, 80 μm, 40 μm, 20 μm, 10 μm, and 5 μm. Here, the PSI grating was placed directly on the face of the detector enclosure (12 mm from detector face to active area) and the image was acquired at 30 seconds intervals with 1093 iterations (total of 9 h of exposures). A non-centroided image demonstrates the previous resolution limitation of the Medipix detector system.

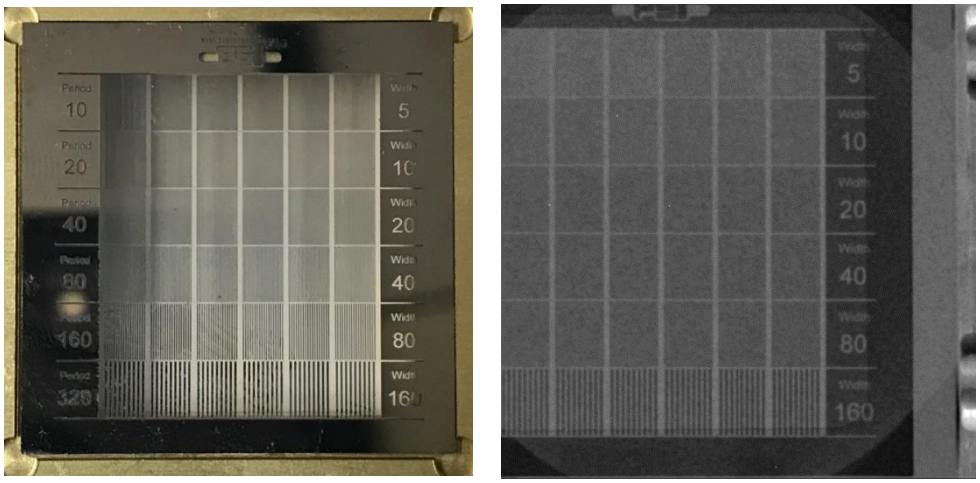

(**a**) (**b**)

Figure 11: Photograph of PSI resolution grating (**a**). Non-centroided neutron image of the PSI resolution grating, comprised of SiO_2 glass backing and 5μm thick Gd absorber with laser-etched test patterns (**b**).[19, 20]

The non-centroided PSI grating (Figure 12a) was compared to the energy resolved centroided image as shown in Figure 12. The radiograph was adjusted with open beam and scaled to represent percentage of neutrons transmitted through the sample. A 9-hour exposure provides sufficient statistics to separate the 20 μm width line pairs with cold neutrons (Figure 12c). The thermal neutron energy radiograph (Figure 12d) can resolve the 20μm width line pairs whereas the contrast for epithermal neutrons suffers due to lower absorption cross section of Gd, i.e., the grating becomes transparent (Figure 12e). The contrast is weaker for the centroided image of all energies (Figure 12b) resembling a white neutron beam weighed by the moderator spectrum, illustrating the benefit of energy-resolved neutron imaging to pick the energy range with the best contrast for a given problem.

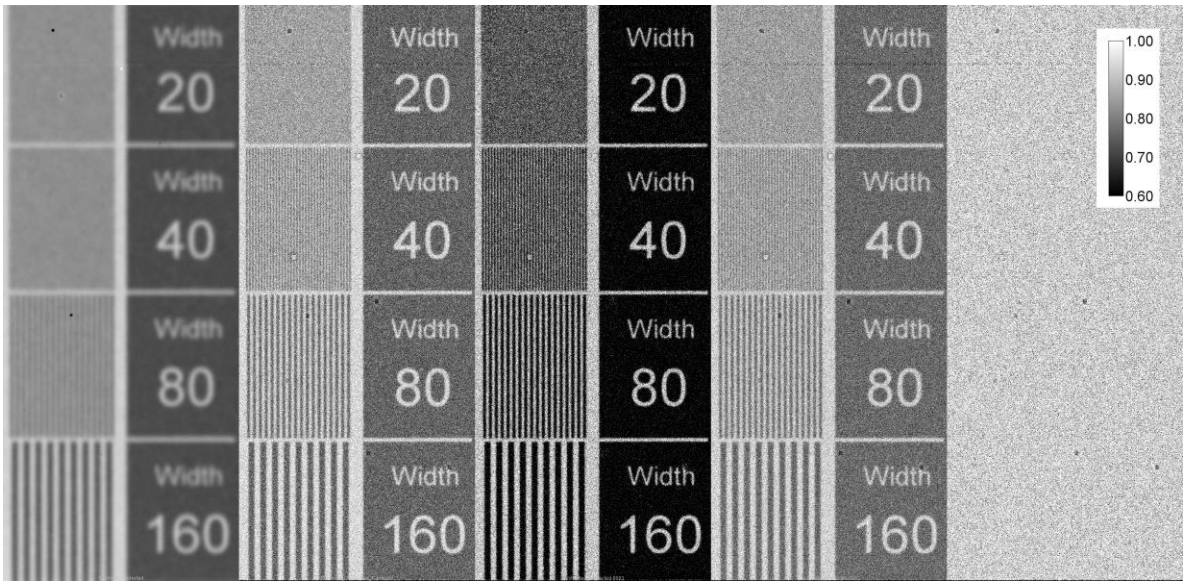

(**a**) (**b**) (**c**) (**d**) (**e**)

Figure 12: Radiograph of PSI grating for original 55 μm original pixel size (**a**). Centroided image with 11 μm effective pixel size for entire energy range of neutrons summed together (**b**) Centroided image with 11 μm effective pixel size for cold (**c**), thermal (**d**), and epithermal (**e**) neutrons.

Figure 13 illustrates multiple fast Fourier transform peaks on a single scatter plot. The peaks have been converted to correspond from pixel/cycle to resolution using the width pairs on the PSI grating. The centroided fast Fourier transform peaks are visible to the 20 μm limit regardless of energy dependence for the processing. The original unprocessed radiograph compared to the centroided counterpart cannot resolve lower than the 80 μm peak whereas the centroided image can resolve 20 μm.

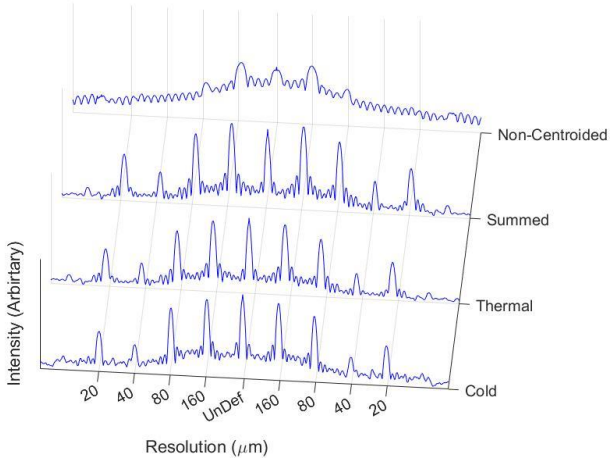

Figure 13: The fast Fourier transform for centroided cold, thermal, non-energy resolved, and raw non-centroided radiographs.

To investigate the resolution as a function of neutron energy, finer energy bins were processed, as shown in Figure 14, ranging from 6 meV to 100 meV. For each energy bin, the contrast resolution was calculated. The contrast resolution (C) is defined as the signal ratio between the dark (S_d) and light(S_l) regions resulting from line width pairs on the grating.[21] Here, the 80 μm line width pairs were chosen, due to the non-centroided radiograph not resolving the 40 μm line width pairs.

$$C = \frac{(S_d - S_l)}{(S_d + S_l)}$$

While contrast resolution is not strictly equivalent to spatial resolution, it is a good indicator of the ability to measure the differences in intensities that define features such as edges in a radiograph, thus quantifying the quality of the image. With increasing neutron energy, the cross section for the gadolinium decreases, resulting in the contrast ratio decreasing to the point where the grating is no longer visible (red marker limit on graph). The centroided image has a higher contrast ratio when compared to the non-centroided image over the entire energy spectrum.

The trend of the decrease in contrast resolution with increasing energy correlates directly with the neutron cross section of gadolinium, suggesting that the contrast resolution is dependent on the sample material only. To illustrate this point, the boron neutron cross section, representing the detector efficiency, is also overlaid in Figure 14. The boron that is inherent in the MCP does not correlate between the contrast resolution of the sample and the boron cross section.

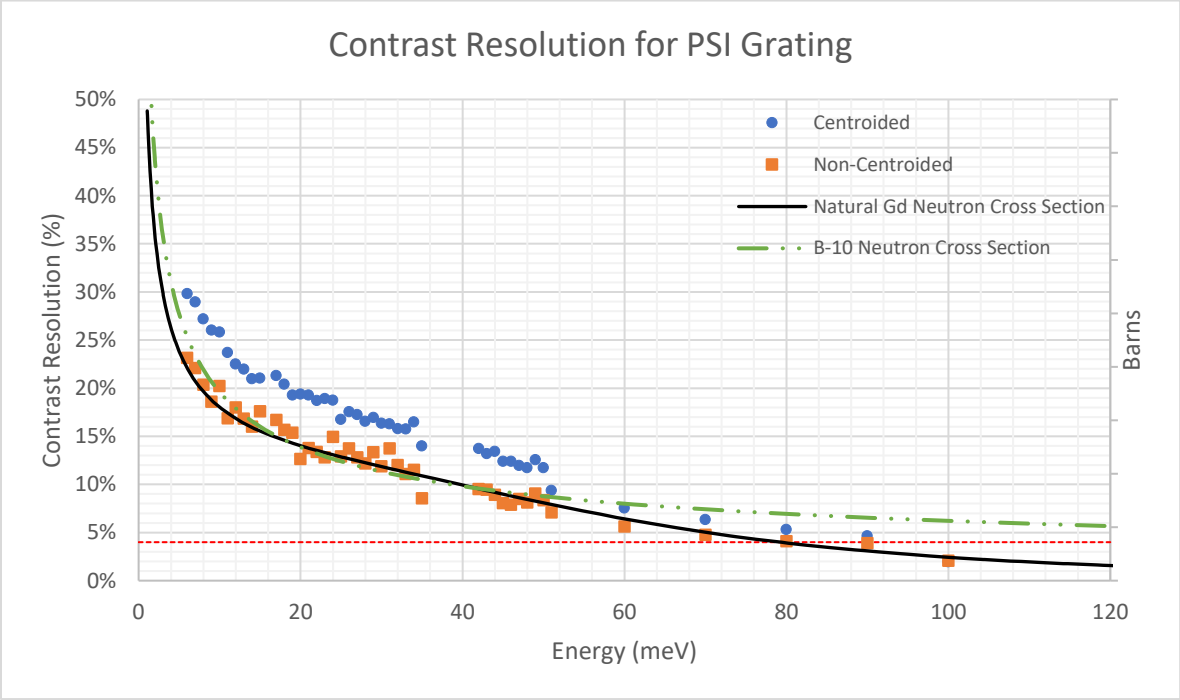

Figure 14: The contrast resolution for finer energy bins ranging from 6 meV to 100 meV. The grating is no longer visible at a contrast of 4% (dashed red). The Gd (solid black) neutron cross sections are compared to the trend of the contrast resolution

The highest possible spatial resolution of the system, assuming perfect counting statistics, can be found by taking the modulation transfer function (MTF) at 10% of a slant edge function. The American Section of the International Association for Testing Materials (ASTM) standard E545 provides information on characterizing neutron beam and image quality by imaging a lead disk, boron nitride disk, and a cadmium wire setup

[**Error! Reference source not found.**]. The design of the imaging standard is reproduced in Figure 5.

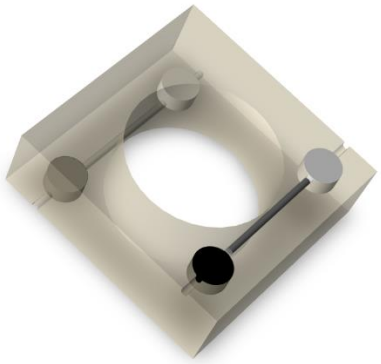

Figure 5: Association for Testing Materials (ASTM) E 2003 standard services after 3d modelling that consists of polytetrafluoroethylene body, 99.9% cadmium wire, 99.9% lead disk (black), and 40% elemental boron nitride disk (white).[22]

The MTF of an imaging system is defined by the absolute value of its optical transfer function and is limited at the high end by the Nyquist frequency.[23] The limiting spatial resolution is considered to be when the MTF crosses 10% since a single sinusoidal wave needs two adjacent pixels to display a full cycle. The Nyquist frequency is then always 0.5 cycles per pixel (or twice the size of one pixel). To obtain the MTF, the cadmium wire provides an edge to produce an edge spread function. The edge spread function is differentiated to obtain the line spread function. The MTF is calculated by taking the Fourier transform of the line spread function. The standard non-centroided and energy resolved centroided radiographs of the ASTM standard object are shown in Figure 6. The processed radiographs confirm a resolution in agreement with the determination with the PSI grating. The MTF at 10% shows that the resolution of the radiographs could be further increased with better counting statistics.

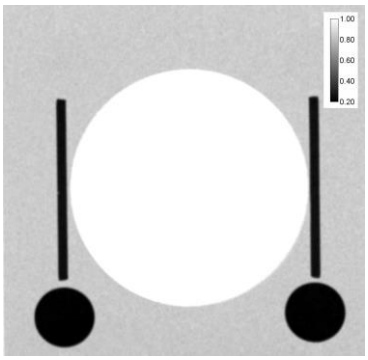

(**a**)

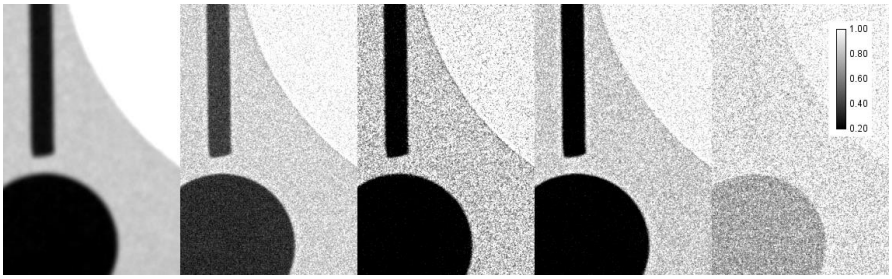

(**b**) (**c**) (**d**) (**e**) (**f**)

Figure 6: Non-centroided image with original 55 μm pixel size imaging ASTM beam purity standard with entire spectrum of neutrons, resulting in ~80 μm resolution (**a**,**b**). Centroided image with 11 μm effective pixel size for entire energy range of neutrons summed together (**c**). Centroided image with 11 μm effective pixel size and with ~40 μm spatial resolution for each cold (**d**), thermal (**e**), and epithermal (**f**) neutrons. The cadmium wire at the epi-thermal energy is almost completely transparent, signifying a decrease in neutron cross section in the higher energy regime.

The MTF is plotted vs spatial frequency for the ASTM standard radiographs (Figure 7). To obtain resolution in μm, cycles/pixel must be converted to line pairs/mm first by using the pixel pitch size. The resolution can now be determined by converting line pairs/mm to μm at 10% on the MTF curve. The non-centroided radiograph results in the highest possible resolution of 70 μm, consistent with the results of the PSI grating where the 80 μm width pairs are barely resolved. The cold neutron energy centroided region results in a resolution of 29 μm and the thermal region results in 22 μm. Using the measured data and sub-pixel size of 11 μm, this cannot be any higher at this point due to the Nyquist frequency being the size of *t*wo pixels, or 22 μm. Epithermal resolution was

not calculated due to low statistics and more importantly the lack of attenuation from the gadolinium precluding a reliable calculation of the edge spread function. An element with a higher cross section in the epithermal energy region to provide an edge is needed to quantify spatial resolution in the epithermal energy range.

The original non-centroided radiograph does not conform to the traditional Nyquist frequency rule-of-thumb (twice the pixel size of 55 μm) due to charge overlap between pixels and can give a resolution below the Nyquist frequency which was determined with the PSI grating to be 80 μm. Since the non-energy resolved radiograph is just the cold, thermal, and epithermal summed together, the resolution for the MTF is degraded by the addition of the epithermal regime. The MTF provides a more exact resolution at which the image can be resolved when compared to the PSI grating. The PSI grating only has very coarse step wedges and there is not an adequate edge for measuring the edge spread function. For the ASTM standard, the thermal range has a better resolution than the cold range due to the penetration of the neutrons through the material which is not seen with the PSI grating. The Gd in the grating effectively blocks all neutrons within the thermal and cold region, whereas, with the standard introduces a scattering medium of polytetrafluoroethylene.

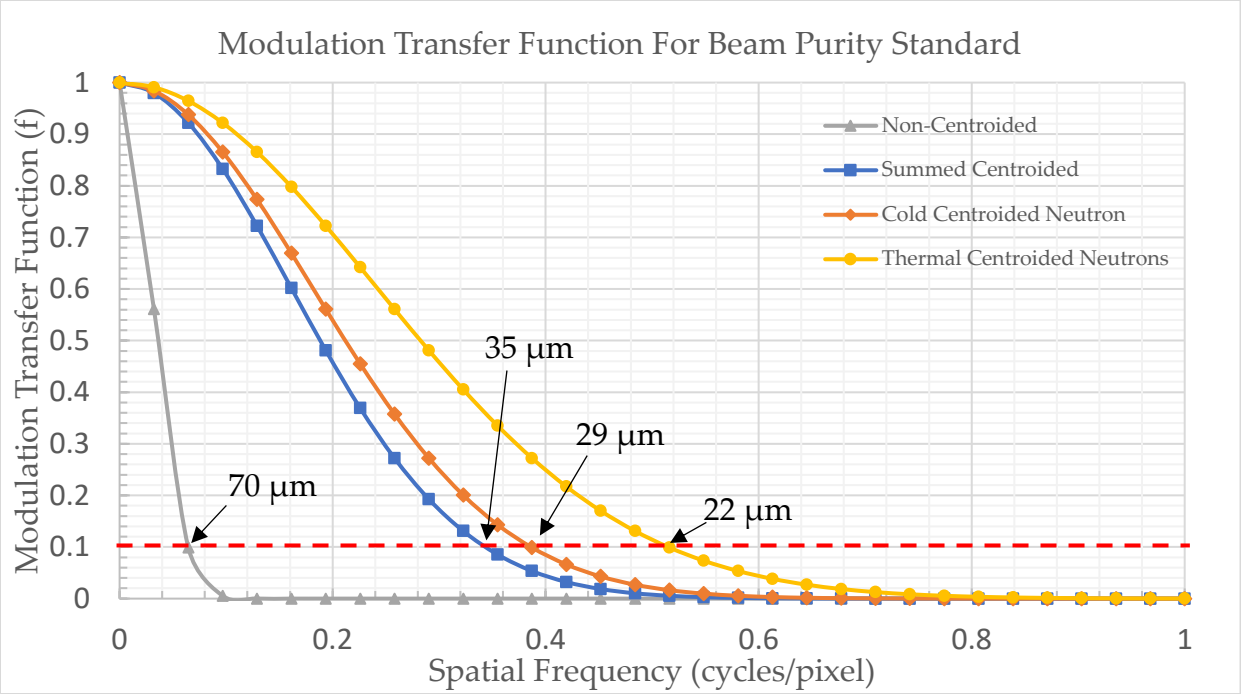

Figure 7: Modulation Transfer Function plots for non-centroided, centroided cold, thermal, and non-energy resolved centroided radiographs. Optimum resolution calculated using MTF at 10% (red dashed line)

3.2 Thermal Scatter Rejection

3.2.1 Experimental Results

The mutli-channel plate collimator that is used downstream from the object to act as a scatter rejection disk is constructed with gadolinium doped borosilicate glass. The wells are etched 8µm in diameter and spaced with 2µm walls in a honeycomb pattern. The collimator is 33mm in diameter and 1mm thick and is doped with 6.8% enriched boron (10B) as well as 10% natural Gd.

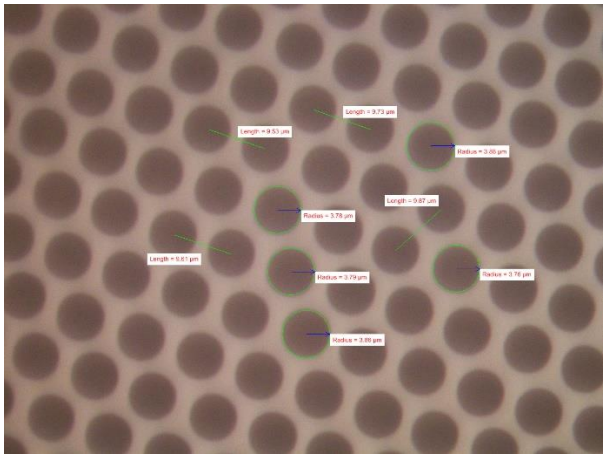

Figure 23: Nova Scientific neutron collimator view under microscope.

The imaging setup is similar to that with event centroiding. The neutron scatter rejection collimator is aligned behind the ASTM standard and increasing amount of scattering material (0cm, 1cm, and 2 cm of acrylic). The transmission of neutrons through the material was calculated by normalizing the open area of the ASTM to 1. A line plot across the borated polyethylene disk gives a defined edge to see increase in spatial resolution (the more pixels between high and low edge, the worse the resolution) and the contrast resolution between scatter and no scatter images.

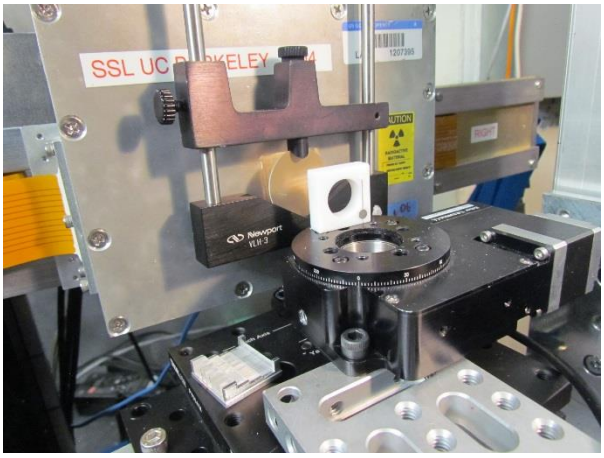

Figure 24: Neutron scatter rejection sample setup with Medipix detector

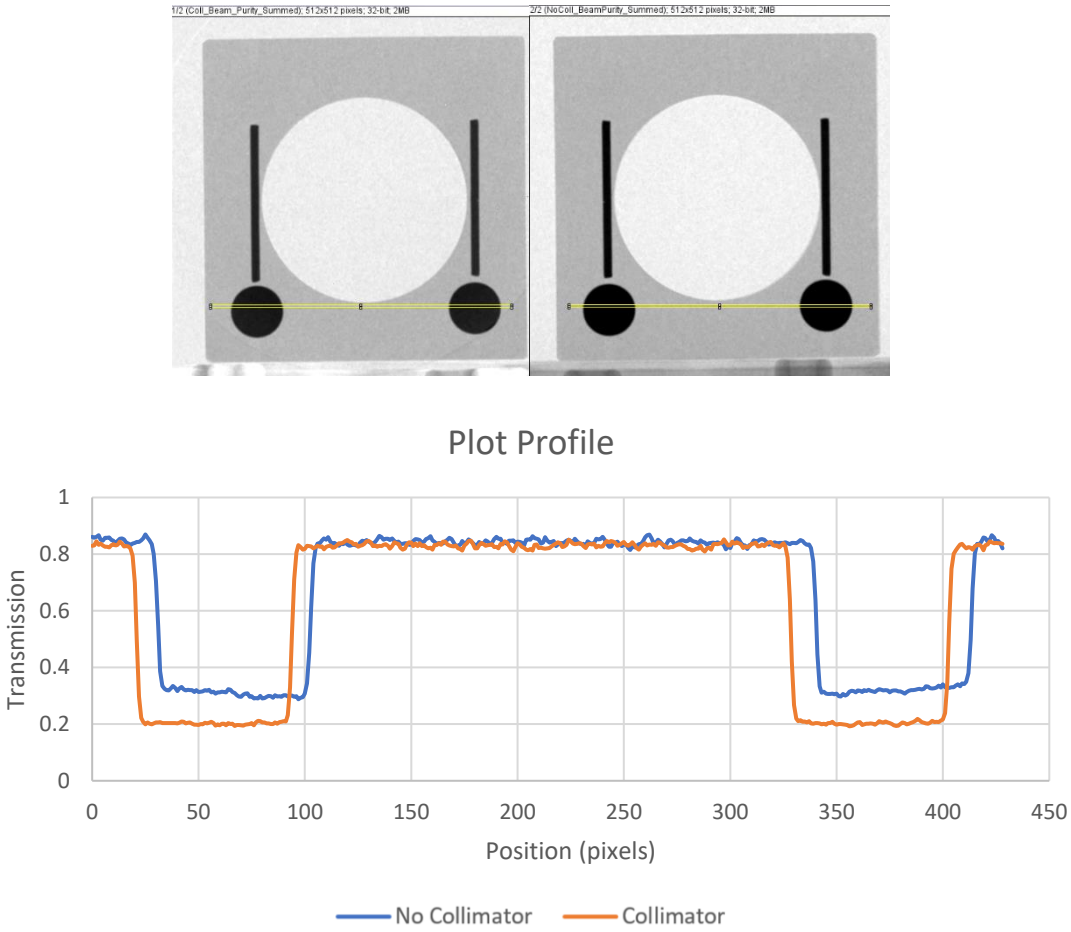

Figure 25: Collimator (upper left) and No Collimator (upper right) transmission plot across boron disk with no added hydrogenous scattering material.

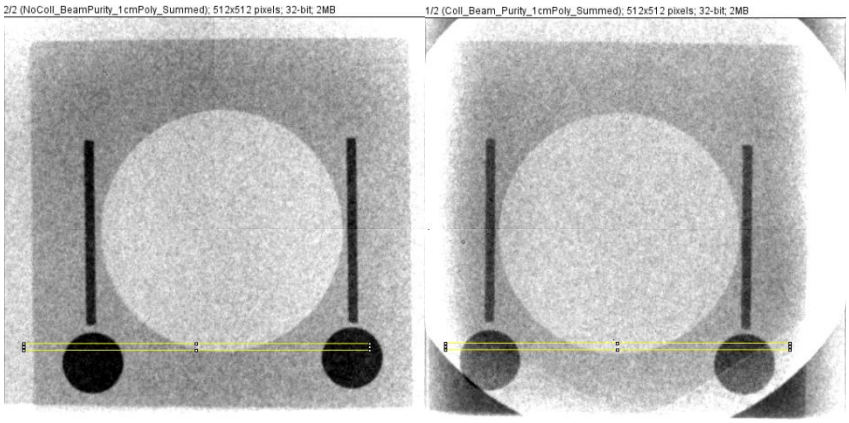

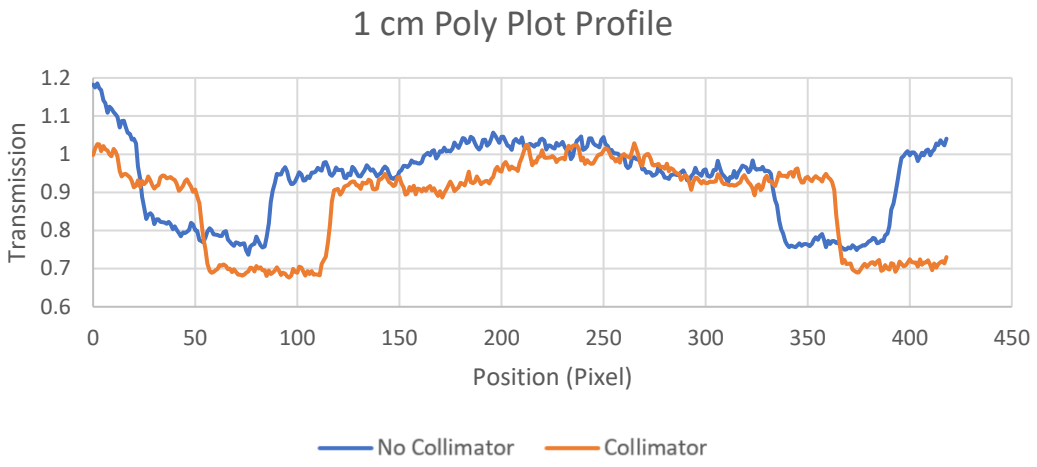

Figure 26: Collimator (upper left) and No Collimator (upper right) transmission plot across boron disk with 1cm added hydrogenous scattering material.

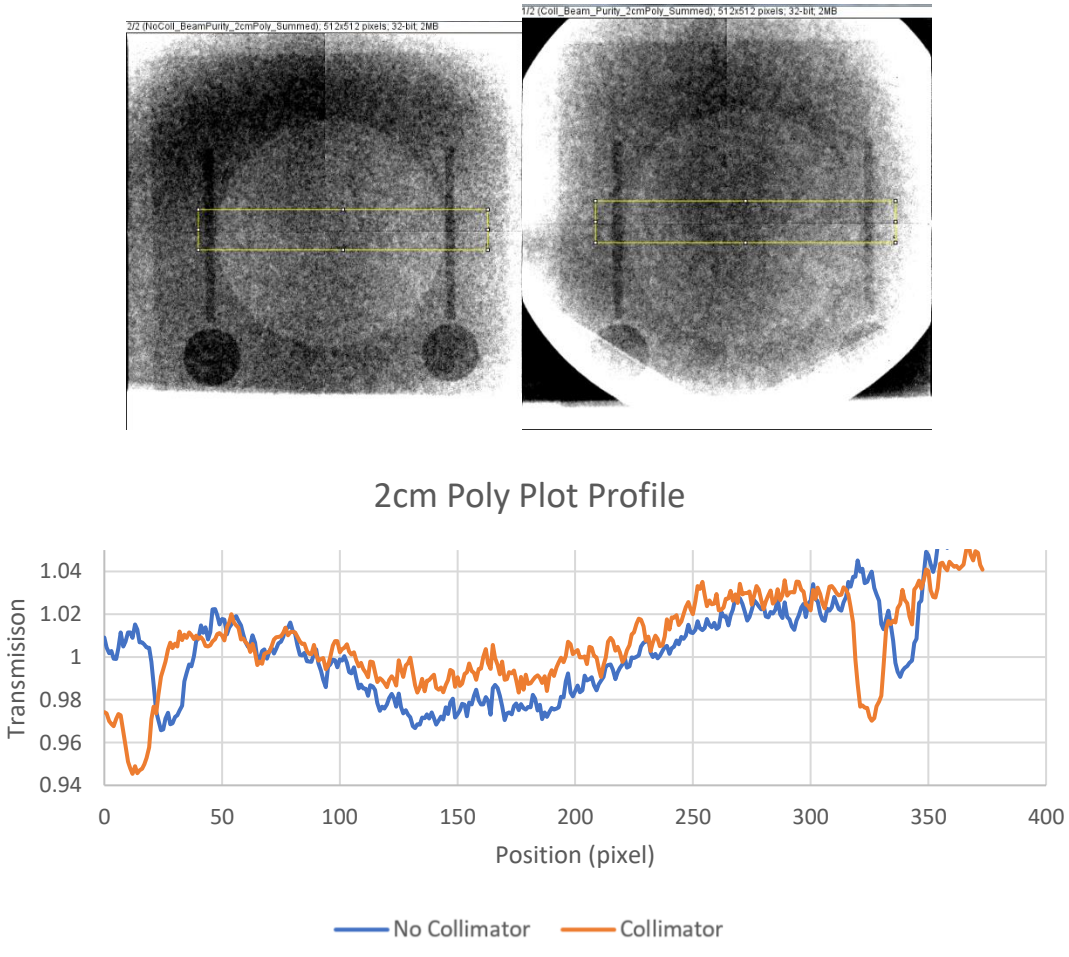

Figure 27: Collimator (upper left) and No Collimator (upper right) transmission plot across boron disk with 2cm added hydrogenous scattering material.

The difference in the borated polyeythlene between a scatter rejected image and non-scattered rejected image shows an increase between 5%-10% change in contrast resolution depending on the thickness of acrylic added to the ASTM standard. That difference in contrast resolution continued while adding more hydrogenous material which is a good indication that using a collimator will improve the contrast between a high absorbing material and a neutron transparent material.

3.2.2 Monte Carlo Analysis

The experiment was confirmed by modeling the exact beam spectrum in MCNP and comparing the transmission through the borated polyethylene disk. Figure 28 demonstrates that there is a difference in the transmission between having a collimator to reject scatter and not having a collimator. The image also shows that while there is an increase in contrast resolution, there isn't exactly an increase in spatial resolution in the setup.

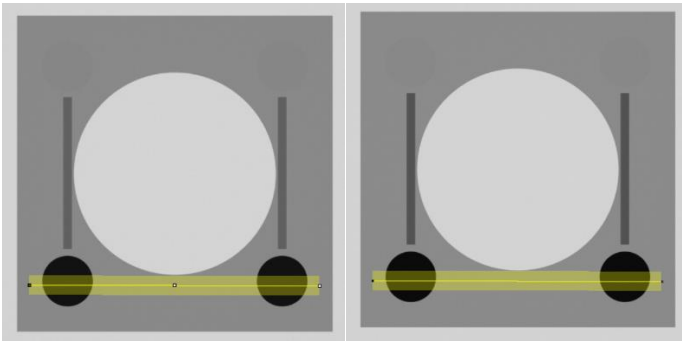

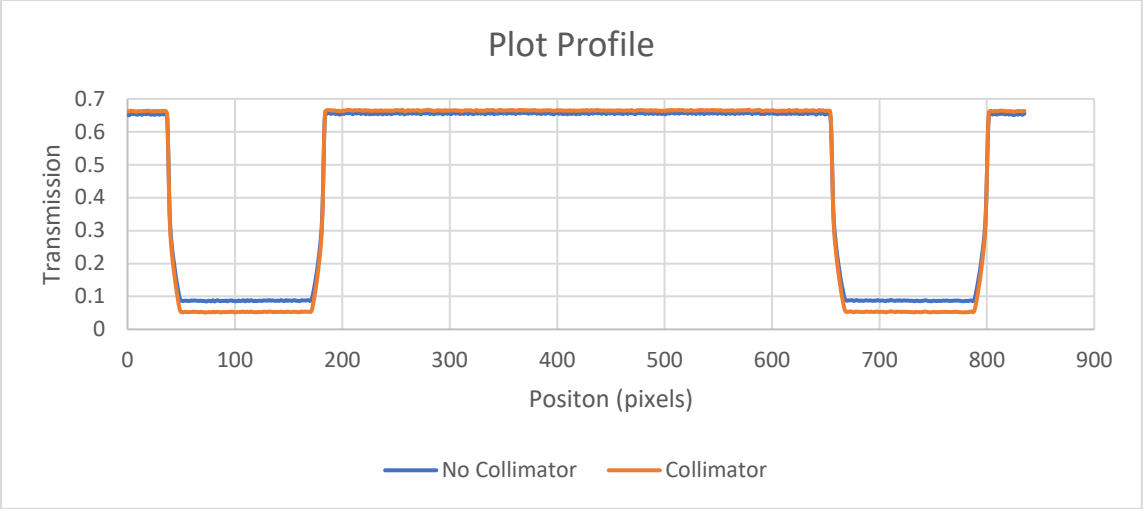

Figure 28: MCNP simulation of the LANL FP5 neutron imaging setup Collimator (upper left) and No Collimator (upper right) transmission plot across boron disk.

The PSI grating was also imaged at FP-11 within the LANSCE facility to assess the scatter rejection quality with a neutron beam consisting of only cold and thermal neutrons. This will remove any doubt that higher energy neutrons are degrading the image. The setup consists of an affordable CMOS detector with a pixel size of 2.4 µm and a LiF/ZnS scintillator screen that has a natural resolution of around 50 µm. The PSI grating was setup with a step wedge of 2mm, 4mm, and 6mm of scattering acrylic, the experiment was conducted with and without the collimator (see Figure 29).

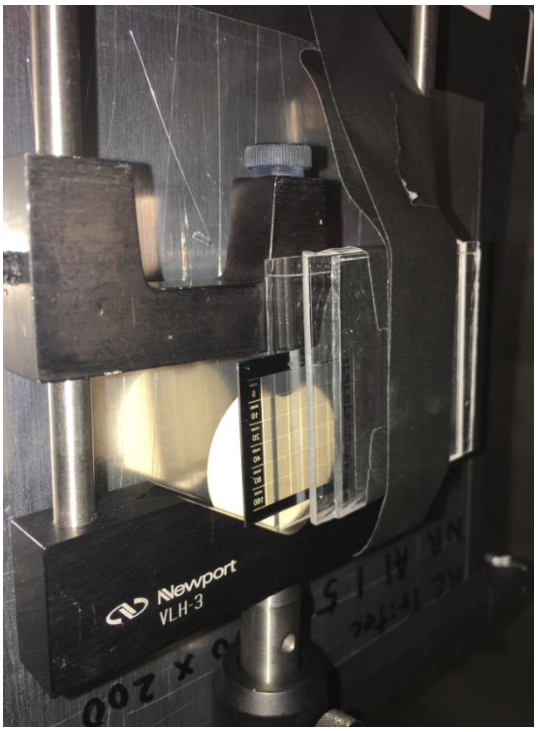

Figure 29: Imaging setup on FP-11 (ASTERIX) with scatter rejecting collimator, scattering medium, and the PSI resolution grating.

Figure 30 illustrates the image quality between PSI grating with and without the scatter rejection. Initially, the non-collimated image has a higher resolution with no scattering material, but with 6mm of scattering material the collimated image was able to resolve the 160 μm lines after adjusting the contrast in the image.

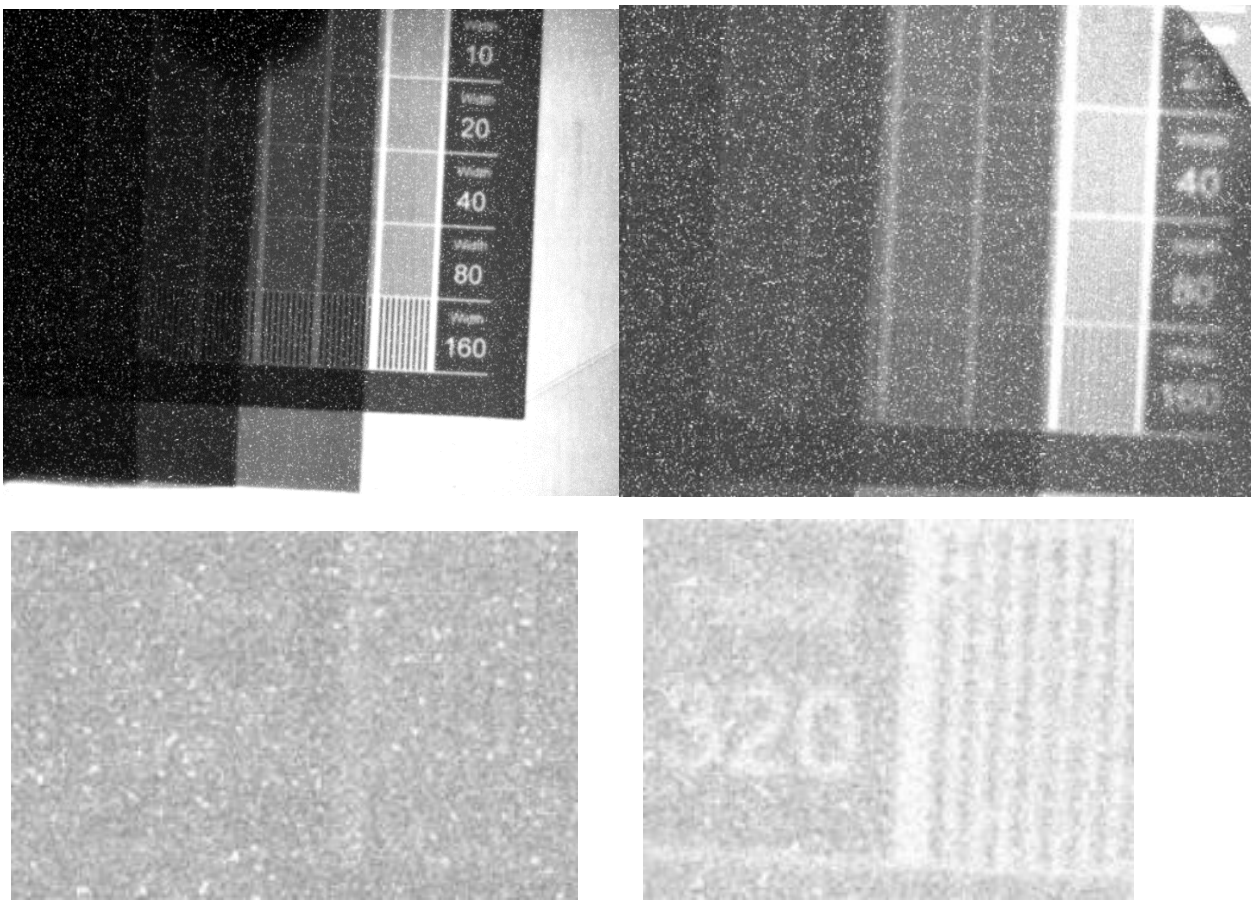

Figure 30: PSI grating without collimator (top left) and with collimator (top right). The zoomed in 160 μm line pairs with 6mm acrylic without collimator (bottom left) and with collimator (bottom right).

Conclusion

With event centroiding we are limited to imaging with higher number of subpixels that will allow the Nyquist frequency limit to go down and provide higher resolution images. Applying centroiding improves overall resolution, but is limited by the incident neutron flux, in the channel size by the MCP, and the event rate that the CMOS chip can handle. One solution would be to increase the number of iterations for each image, but the centroiding pattern effect, visible in the inset of Figure 15a, would only get worse with more subpixels. With proper software and hardware implementation, event centroiding

can be conducted in parallel with the data acquisition. Spatial resolution was improved by a factor of ~4 using event centroiding compared to the non-centroided results, implying a similar resolution improvement for tomography. For the ASTM standard, the spatial resolution was better for the thermal neutrons versus the cold neutrons, while the test object did not provide enough contrast for the epithermal neutrons. The thermal flux is higher than that of the cold neutrons so the amount of events on detector provide better statistics for the same imaging time. Thus cold neutrons typically will give higher resolution than thermal neutrons for thin enough samples. With the current characterization samples, based on gadolinium contrast, we were able to quantify the contrast resolution as a function of energy. The contrast resolution increased by 7% with the centroiding process. The energy dependence scaled with the gadolinium cross section allowing to conclude that the contrast resolution mostly depends on the sample material and not on incident flux or detector properties. In the near future, the method will be applied to nuclear fuel pellets to attempt the demonstration of the improved spatial resolution for isotope quantification. This will also allow us to assess the spatial and contrast resolution for a larger energy range.

The thermal neutron scatter rejection images demonstrate that there is an increase in contrast resolution but not necessarily increased spatial resolution. When increasing the amount of hydrogen in the object, the contrast resolution decreases but is still better than the non collimator setup by 5%. The comparison between the LANSCE energy spectrum and the MCNP coincides that overall the contrast resolution does increase when there is hydrogen scatter present. Unfortunately, this experiment did not illuminate the benefit of scatter rejection increasing spatial resolution. There was no increase in spatial resolution between the images due to the possibility that there wasn't a pure thermal beam and the collimator could not reject the scatter from epithermal and fast neutrons. This was confirmed by conducting the experiment at the ASTERIX beamline as well. The

absence of epithermal and fast neutrons confirmed that with a collimator the 160 μm line width pairs are visible with 6mm of acrylic and was not without the collimator.

Discussion

5.1 Improving Future Experiments

5.1.1 Collimator Alignment

The collimator has a transmission tolerance of about 1 degree. This results in the need to adjust the collimator in no greater than 0.5 degree steps to find the incident beam. To align the collimator at LANSCE, the whole process took around 15 hours of searching. The beam will block 90% of the neutrons incident to the target sample when it is oblique in the alignment. When correctly aligned, 75% of neutrons pass through the collimator and make it to the sample. This value isn't 100% due to the wall thickness between the holes in the collimator allow the packing fraction of 75% open to holes (as seen in figure 31 A, B, C).

A

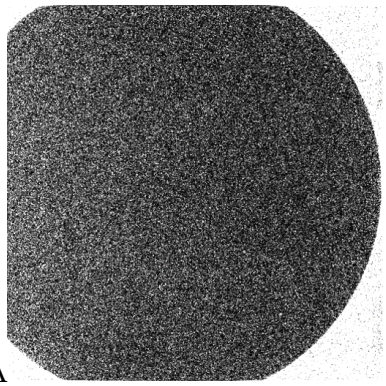

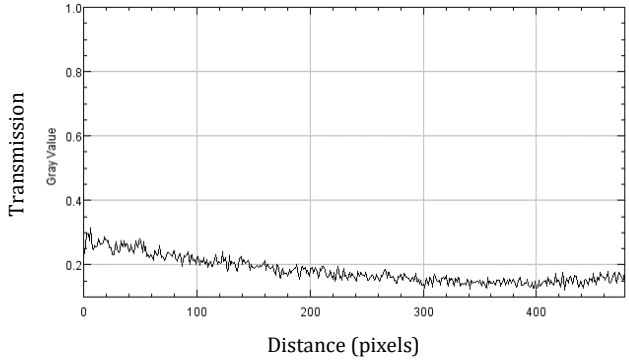

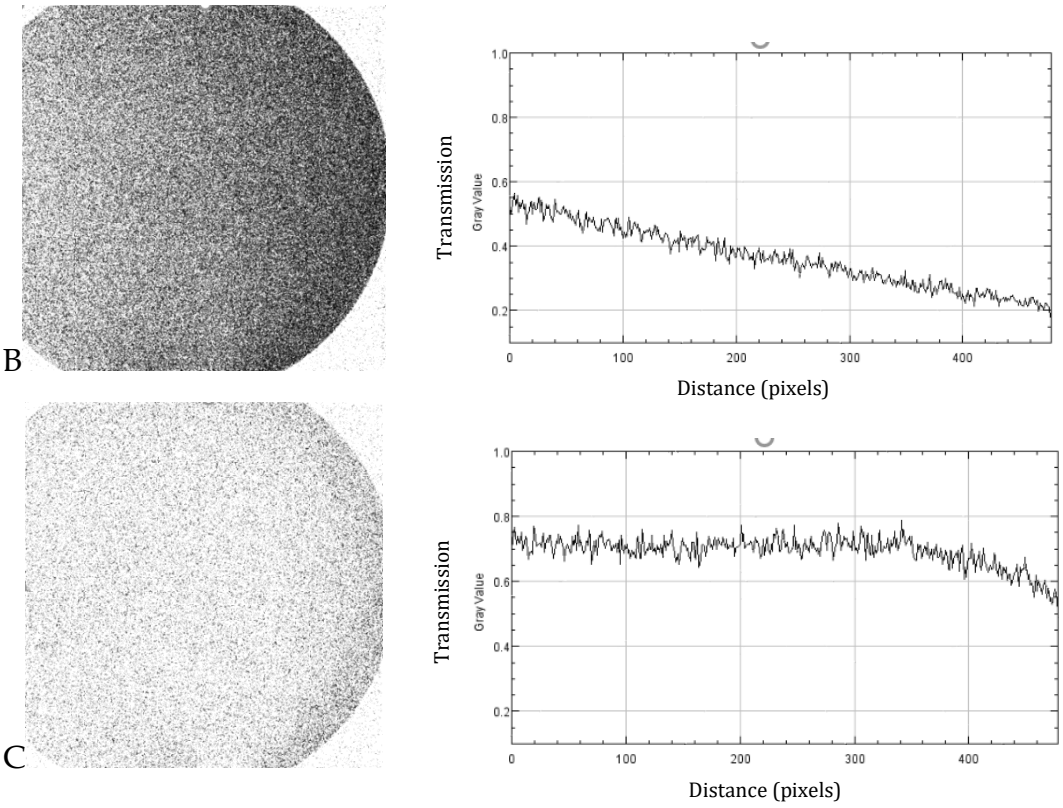

Figure 31: Alignment of the Nova Scientific collimator at the LANSCE FP5 facility.

5.1.2 Higher Energy Neutrons

The limitation of neutron imaging biological material is the amount of hydrogen in the sample. The range of thermal neutrons and the amount of scattered neutron radiation produced in tissue limit the utility of this modality to be used in humans. The range of thermal neutrons in tissue is no more than a couple centimeters. Increasing the range in tissue is fairly simple by using higher energy neutrons. One issue with higher energy neutrons is the properties of interaction within tissue and the detector collection scintillator changes as the energy increases. Also, the collimator effectiveness in the

epithermal and fast neutron range is diminished and a new collimator will need to be explored with a possible cadmium coating as well..

5.1.3 Adelphi Generator

Moving further away from the neutron source provides a more collimated and parallel beam. Issues with the portable neutron generator are that these is no beam column to collimate the beam and increase the distance from the source. Also, the generator is not properly shielded and emits neutrons in all directions. Due to these issues, placing the sample at 1 meter away from the generator yeilds 0.5mm resolution (shown in figure 32). Improving beam imaging quality of the neutron generator will allow labs to neutron image without the need to visit a national lab or nuclear reactor.

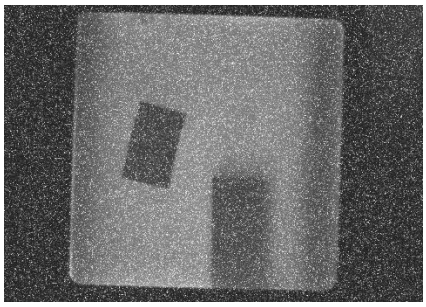

Figure 32: Illuminated scintillator with Gd foil (left) and borated polyethylene (right).

Appendex A
Code for Condensing Medipix Data

```
#!/bin/bash

while true
do
```

```
startTime=$(date +%s)

#echo "run(\"Image Sequence...\", \"open=ReplaceWithPathName\\\\ReplaceWithFileName number=146 starting=1 increment=1 scale=100 file=ReplaceWithFileRunNumber sort\");" > MacroCentroid.ijm
#echo "run(\"Save\", \"save=ReplaceWithPathName\\\\FullFile.tif\");" >> MacroCentroid.ijm
#echo "close();" >> MacroCentroid.ijm
#echo "run(\"Quit\");" >> MacroCentroid.ijm

count=`ls -1 *_00000.fits 2>/dev/null | wc -l`

if [ $count != 0 ]
then

        echo "--> found new files!"
        files=`ls *_00000.fits`
        echo "--> Lets wait three minutes to make sure files were fully saved..."
        sleep 10


        for f in $files
        do
         shortName=`echo $f | tail -c 15 | gawk -F"_" '{print $1}'`

         echo "--> Processing run $shortName"

         pathName=$(cygpath -w $PWD | sed -e 's/\\/\\\\\\\\\\\\/g')

        sed -e s/ReplaceWithFileName/$f/g MacroCentroid.ijm | sed -e s/ReplaceWithFileRunNumber/"$shortName"_0/g | sed -e s/ReplaceWithPathName/"$pathName"/g > Macro"$shortName"Temp.ijm

         echo "--> Starting ImageJ script"

         echo "Imagej --headless -macro Macro"$shortName"Temp.ijm"
```

```
        #Imagej -macro Macro"$shortName"Temp.ijm
        Imagej --headless -macro Macro"$shortName"Temp.ijm

        echo "--> finished ImageJ script. Cleaning up..."

        tifName=${f::(-11)}

        #mv CentrFile.tif $tifName"_Centr.tif"



        mv 400meVCentrFile.tif $tifName"_400meVCentr.tif"
        mv 025meVCentrFile.tif $tifName"_025meVCentr.tif"
        mv 006meVCentrFile.tif $tifName"_006meVCentr.tif"



        echo "--> removing $tifName files"

        #uncomment the line below if you'd like to safe each recorded stack for post processing
        mv FullFile.tif $tifName".tif"

        rm "$tifName"*0*.fits
        rm "$tifName"*.txt

       done

        rm *Temp.ijm
       # rm MacroCentroid.ijm

       endTime=$(date +%s)

       echo "-> Time elapsed: $(($endTime - $startTime))s"

fi
echo "--> No new files found!"
```

```
echo "Press [CTRL+C] to stop.."
sleep 5
done
```

Code for Centroiding in ImageJ

```
setBatchMode(true);
run("Set Measurements...", "centroid redirect=None decimal=3");
run("Image Sequence...", "open=ReplaceWithPathName\\ReplaceWithFileName starting=1 increment=1 scale=100
file=ReplaceWithFileRunNumber sort");
run("Save", "save=ReplaceWithPathName\\FullFile.tif");
imageName=getTitle();
run("Max...", "value=1 stack");
setThreshold(0, 0);
setOption("BlackBackground", true);
run("Convert to Mask", "method=Default background=Dark");


//First set of data down to 400meV
selectWindow(imageName);
run("Make Substack...", "  slices=1-675");
run("Analyze Particles...", "size=2-20 display clear stack");
newImage("empty", "32-bit", 2560, 2560, 1)
for(n = 0; n < nResults; n++)
{

xvalue=getResultString("X", n);
yvalue=getResultString("Y", n);
//print (n, xvalue,yvalue);
xcoord=round(xvalue*5);
ycoord=round(yvalue*5);
curVal=getPixel(xcoord,ycoord);
   setPixel(xcoord,ycoord,curVal+1);
   //makeRectangle(round(xvalue*4), round(yvalue*4), 1, 1);
```

```
   //run("Add...", "value=1");
   showProgress(n, nResults);
}
run("Grays");
run("Save", "save=ReplaceWithPathName\\400meVCentrFile.tif");

//First set of data from 400meV down to 25meV
selectWindow(imageName);
run("Make Substack...", "  slices=676-2421");
run("Analyze Particles...", "size=2-20 display clear stack");
newImage("empty", "32-bit", 2560, 2560, 1)
for(n = 0; n < nResults; n++)
{

xvalue=getResultString("X", n);
yvalue=getResultString("Y", n);
//print (n, xvalue,yvalue);
xcoord=round(xvalue*5);
ycoord=round(yvalue*5);
curVal=getPixel(xcoord,ycoord);
   setPixel(xcoord,ycoord,curVal+1);
   //makeRectangle(round(xvalue*4), round(yvalue*4), 1, 1);
   //run("Add...", "value=1");
   showProgress(n, nResults);
}
run("Grays");
run("Save", "save=ReplaceWithPathName\\025meVCentrFile.tif");



//First set of data from 25meV down to 6meV
selectWindow(imageName);
run("Make Substack...", "  slices=2422-3197");
run("Analyze Particles...", "size=2-20 display clear stack");
newImage("empty", "32-bit", 2560, 2560, 1)
```

```
for(n = 0; n < nResults; n++)
{

xvalue=getResultString("X", n);
yvalue=getResultString("Y", n);
//print (n, xvalue,yvalue);
xcoord=round(xvalue*5);
ycoord=round(yvalue*5);
curVal=getPixel(xcoord,ycoord);
   setPixel(xcoord,ycoord,curVal+1);
   //makeRectangle(round(xvalue*4), round(yvalue*4), 1, 1);
   //run("Add...", "value=1");
   showProgress(n, nResults);
}
run("Grays");
run("Save", "save=ReplaceWithPathName\\006meVCentrFile.tif");

run("Quit");
setBatchMode(false);
//updateResults;
```

Code for MCNP for Beam Purity Indicator with Collimator

```
BPI Imaging Standard without Collimator
c ***************** BLOCK 0: Overview ************************************
c
c ***************** BLOCK 1: CELL CARDS **********************************
c
```

```
c Center Hole In BPI Block
101    4   -1.20479E-03   (-1006 1004 -1005)   imp:n = 1
c
c BPI Standard Discs Flush with Front Face
3010   7   -11.35    (-3010 -1005 3012)   imp:n = 1
3011   1   -2.100    (-3011 -1005 3012)   imp:n = 1
c
c BPI Standard Discs Flush with Rear Face
3020   7   -11.35    (-3020 -3022 1004)   imp:n = 1
3021   1   -2.100    (-3021 -3022 1004)   imp:n = 1
c
c BPI Standard Rod on Front Face
3030   6   -8.650    (-3030 3031 -3032)   imp:n = 1
c
c BPI Standard Rod on Rear Face
3040   6   -8.650    (-3040 3031 -3032)   imp:n = 1
c
c BPI Block
100    2   -2.200    (1000 -1001 1002 -1003 1004 -1005)
     #101 #3010 #3011 #3020 #3021 #3030 #3040
     imp:n = 1
c
c
c Collimator Block
2000   0   (-2000 2001 2002 -2003 2004 -2005)
     FILL=1
     imp:n = 1
2001   0   2010 -2011 2012 -2013
     u=1 FILL=2 LAT=1
     imp:n = 1
2002   4   -1.20479E-03   (-2014)
     u=2
     imp:n = 1
2003   3   -2.650   (2014)
     u=2
```

```
    imp:n = 1
c
c
c Imaging Plate
4000   0   (-4000 4001 4002 -4003 4004 -4005)
    imp:n = 1
c
c Volume Above Block Inside End of World Sphere
200   4   -1.20479E-03   (-1 1005)
    imp:n = 1
c
c Volume Below Block Inside End of World Sphere
201   4   -1.20479E-03   (-1 -4001)
    imp:n = 1
c
c Volume Around BPI Block Z-plane limits
202   4   -1.20479E-03   (-1 1004 -1005)(-1000:1001:-1002:1003)
    imp:n = 1
c
c Volume Gap Between BPI Block and Collimator
203   4   -1.20479E-03   (-1 -1004 2000)
    imp:n = 1
c
c Volume Around Collimator Z-plane limits
204   4   -1.20479E-03   (-1 -2000 2001)(-2002:2003:-2004:2005)
    imp:n = 1
c
c Volume Gap Between Collimator and Imaging Plate
205   4   -1.20479E-03   (-1 -2001 4000)
    imp:n = 1
c
c Volume Around Imaging Plate Z-Plane Limits
206   4   -1.20479E-03   (-1 -4000 4001)(-4002:4003:-4004:4005)
    imp:n = 1
c
```

```
c End of World Sphere
1   0   (1)   imp:n = 0
c
c Blank line required here.


c ***************** BLOCK 2: SURFACE CARDS *********************************
c
c BPI Block
1000 PX -1.250
1001 PX  1.250
1002 PY -1.250
1003 PY  1.250
1004 PZ -0.800
1005 PZ  0.000
1006 CZ  0.800
c
c Collimator Block
2000 PZ -0.900
2001 PZ -1.000
2002 PX -1.650
2003 PX  1.650
2004 PY -1.650
2005 PY  1.650
c
c Collimator Grid
2010 PX  0.0000
2011 PX  0.0010
2012 PY  0.0000
2013 PY  0.0010
2014 C/Z 0.0005 0.0005  0.0004
c
c Test Discs Flush with Front Surface
3010 C/Z -0.85 -0.85  0.2
3011 C/Z  0.85 -0.85  0.2
c Use 1005 for top cutoff
```

```
3012 PZ -0.200
c
c Test Discs Flush with Rear Surface
3020 C/Z -0.85  0.85  0.2
3021 C/Z  0.85  0.85  0.2
3022 PZ -0.600
c Use 1004 for bottom cutoff
c
c Test Rod on Front Face
3030 C/X -0.850 -0.035  0.035
3031 PX -0.605
3032 PX  0.595
c
c Test Rod on Rear Face
3040 C/X 0.850 -0.764  0.035
c Use 3031 for lower X plane
c Use 3032 for upper X plane
c
c Imaging Plate
4000 PZ -2.225
4001 PZ -3.225
4002 PX -1.408
4003 PX  1.408
4004 PY -1.408
4005 PY  1.408
c
c End of World Sphere
1 so 550.00
c
c
c Blank line required here.

c ***************** BLOCK 3: DATA CARDS ************************************
c
mode n
```

```
c
c ***************** BLOCK 4: TALLY DEFINITION ******************************
c
FMESH14:n  Geom = xyz  Origin = -1.408 -1.408 -3.225
          IMESH = 1.408   IINTS = 2048
          JMESH = 1.408   JINTS = 2048
          KMESH = -2.225  KINTS = 1
          OUT = col
c
c ***************** BLOCK 5: SOURCE DEFINITION *****************************
c
SDEF   PAR=1   POS=0.00 0.00 500.00   ERG=d1
      x=d2   y=d3   z=0   VEC=0 0 -1   DIR=1
c
SI1 A  1.08273E-09  1.18659E-09  1.30590E-09  1.39589E-09  1.51081E-09
      1.73337E-09  1.90762E-09  2.01371E-09  2.17957E-09  2.38871E-09
      2.58534E-09  2.80995E-09  2.99104E-09  3.26443E-09  3.44590E-09
      3.77653E-09  4.08750E-09  4.35099E-09  4.70926E-09  5.05476E-09
      5.49380E-09  6.09666E-09  6.46279E-09  6.96590E-09  7.44590E-09
      8.09265E-09  8.79562E-09  9.32374E-09  1.01759E-08  1.08770E-08
      1.17726E-08  1.27421E-08  1.37339E-08  1.51147E-08  1.60223E-08
      1.71264E-08  1.88485E-08  2.01477E-08  2.18979E-08  2.36028E-08
      2.57605E-08  2.77660E-08  2.91893E-08  3.18579E-08  3.49157E-08
      3.71671E-08  4.10756E-08  4.44595E-08  4.97532E-08  5.52152E-08
      5.95162E-08  6.30922E-08  6.88628E-08  7.39187E-08  8.06801E-08
      8.69667E-08  9.29649E-08  1.01469E-07  1.08016E-07  1.18390E-07
      1.26031E-07  1.37561E-07  1.48281E-07  1.58509E-07  1.73009E-07
      1.84175E-07  2.02704E-07  2.19409E-07  2.33566E-07  2.54930E-07
      2.70245E-07  2.96193E-07  3.17940E-07  3.42707E-07  3.70948E-07
      3.94872E-07  4.30991E-07  4.70402E-07  5.04938E-07  5.46542E-07
      5.86671E-07  6.35009E-07  6.90205E-07  7.37809E-07  8.05281E-07
      8.60814E-07  9.31741E-07  1.00852E-06  1.08709E-06  1.17176E-06
      1.26305E-06  1.36713E-06  1.49840E-06  1.58843E-06  1.70504E-06
      1.85324E-06  2.01432E-06  2.19855E-06  2.32099E-06  2.53324E-06
      2.73057E-06  2.93104E-06  3.22587E-06  3.44832E-06  3.71691E-06
```

3.94027E-06 4.30066E-06 4.71357E-06 4.99680E-06 5.45378E-06

5.78151E-06 6.31023E-06 6.83014E-06 7.42385E-06 8.13659E-06

8.55400E-06 9.33624E-06 1.01477E-05 1.08475E-05 1.17903E-05

1.26033E-05 1.36987E-05 1.48895E-05 1.60493E-05 1.72996E-05

1.83391E-05 2.00162E-05 2.16656E-05 2.31595E-05 2.50679E-05

2.71333E-05 2.94917E-05 3.19217E-05 3.41227E-05 3.69345E-05

3.96463E-05 4.32722E-05 4.68377E-05 5.02762E-05 5.51032E-05

5.76887E-05 6.34914E-05 6.92975E-05 7.34616E-05 7.91841E-05

8.42922E-05 9.31585E-05

c

SP1 2.28437E+05 2.55487E+05 2.57181E+05 2.65790E+05 2.87639E+05

3.21703E+05 3.39104E+05 3.66976E+05 3.66985E+05 3.85564E+05

4.26982E+05 4.34076E+05 4.68213E+05 4.87084E+05 5.46549E+05

5.81827E+05 6.09273E+05 6.35914E+05 6.68105E+05 6.97321E+05

7.39890E+05 7.82484E+05 7.85077E+05 8.19408E+05 8.49629E+05

8.95583E+05 9.34749E+05 9.59700E+05 1.00497E+06 1.06632E+06

1.12770E+06 1.16545E+06 1.23659E+06 1.28644E+06 1.31644E+06

1.35158E+06 1.36054E+06 1.35610E+06 1.40150E+06 1.43419E+06

1.46283E+06 1.51180E+06 1.51681E+06 1.52185E+06 1.51689E+06

1.51692E+06 1.49221E+06 1.45348E+06 1.40647E+06 1.36547E+06

1.29974E+06 1.23310E+06 1.14702E+06 1.08108E+06 9.92458E+05

9.02149E+05 8.28192E+05 7.57804E+05 6.97972E+05 6.20016E+05

5.56226E+05 4.97363E+05 4.43267E+05 4.04259E+05 3.65064E+05

3.25357E+05 2.97706E+05 2.75105E+05 2.54220E+05 2.34921E+05

2.26574E+05 2.12848E+05 1.99952E+05 1.89078E+05 1.75878E+05

1.72443E+05 1.58307E+05 1.53187E+05 1.44856E+05 1.37883E+05

1.29104E+05 1.23294E+05 1.15824E+05 1.06329E+05 1.01545E+05

9.50789E+04 9.05020E+04 8.44613E+04 7.93442E+04 7.60233E+04

7.09490E+04 6.64315E+04 6.22021E+04 5.90129E+04 5.67293E+04

5.29429E+04 5.02288E+04 4.68764E+04 4.34602E+04 4.16415E+04

3.96368E+04 3.74812E+04 3.52106E+04 3.32957E+04 3.19021E+04

2.97725E+04 2.76941E+04 2.62745E+04 2.46825E+04 2.34173E+04

2.18541E+04 2.08707E+04 1.99972E+04 1.86626E+04 1.77641E+04

1.64695E+04 1.58324E+04 1.49222E+04 1.40642E+04 1.32558E+04

1.26592E+04 1.20499E+04 1.11351E+04 1.06340E+04 1.00227E+04

```
      9.44642E+03  8.96218E+03  8.44697E+03  8.04031E+03  7.52838E+03
      7.18961E+03  6.82104E+03  6.45010E+03  6.15982E+03  5.80570E+03
      5.45395E+03  5.14044E+03  4.86088E+03  4.65744E+03  4.40418E+03
      4.16462E+03  3.93816E+03  3.77336E+03  3.54472E+03  3.36299E+03
      3.19058E+03  2.99731E+03
c
SI2    -3.00   3.00
SP2     0      1
SI3    -3.00   3.00
SP3     0      1
c
c ***************** BLOCK 6: MATERIAL DEFINITION ****************************
c
c Material 1 is min40%Boron Nitride
c Material 1 density is: 2.100 [g/cm^3]
M1   5010 -0.0796   5011 -0.3204
     7014 -0.597792   7015 -0.002208
c
c Material 2 is Teflon (Polytetrafluoroethylene)
c Material 2 density is: 2.200 [g/cm^3]
M2   6012 -0.2376130419   6013 -0.0025699581
     9019 -0.759817
c
c Material 3 is Collimator 10% Nat-Gd, 6.8% B-10, 83.2% SiO2
c Material 3 density is: 2.650 [g/cm^3]
M3   64000 -0.1000
     5010 -0.0680
     14000 -0.38891
     8016 -0.44309
c
c Material 4 is air
c Material 4 density is: 1.20479E-03 [g/cm^3]
M4   6012 -0.0001226732    6013 -0.0000013268
     7014 -0.75248761744   7015 -0.00277938256
     8016 -0.231781
```

```
     18000 -0.012828
     GAS=1
c
c Material 6 is Cd
c Material 6 density is: 8.650 [g/cm^3]
M6   48000 1
c
c Material 7 is Pb
c Material 7 density is: 11.35 [g/cm^3]
M7   82000 1
c
c
c ***************** Energy, Time, and Weight Cutoff *************************
c
c The CUT command specifies the minimum energy, time, or particle weight below
c which the particle is killed.
c Neutrons with energy < 1.00E-10 MeV are killed.
c "1j" jumps over "1" input parameter and uses the default value for the jumped
c paramater (the "time cutoff" in this case).
c
cut:n  1j  1.00E-10
c
c ***************** Physics Simplification *********************************
c
c ***************** NUMBER OF PARTICLE HISTORIES ****************************
nps 1E11
```

Code for MCNP for Beam Purity Indicator Without Collimator

```
Square Neutron Beam only.
c ***************** BLOCK 0: Overview ***************************************
c
```

```
c ***************** BLOCK 1: CELL CARDS ************************************
c
c Center Hole In BPI Block
101    4   -1.20479E-03   (-1006 1004 -1005)   imp:n = 1
c
c BPI Standard Discs Flush with Front Face
3010   7   -11.35   (-3010 -1005 3012)   imp:n = 1
3011   1   -2.100   (-3011 -1005 3012)   imp:n = 1
c
c BPI Standard Discs Flush with Rear Face
3020   7   -11.35   (-3020 -3022 1004)   imp:n = 1
3021   1   -2.100   (-3021 -3022 1004)   imp:n = 1
c
c BPI Standard Rod on Front Face
3030   6   -8.650   (-3030 3031 -3032)   imp:n = 1
c
c BPI Standard Rod on Rear Face
3040   6   -8.650   (-3040 3031 -3032)   imp:n = 1
c
c BPI Block
100    2   -2.200   (1000 -1001 1002 -1003 1004 -1005)
     #101 #3010 #3011 #3020 #3021 #3030 #3040
     imp:n = 1
c
c
c Collimator Block
2000   0   (-2000 2001 2002 -2003 2004 -2005)
     FILL=1
     imp:n = 1
2001   0   2010 -2011 2012 -2013
     u=1 FILL=2 LAT=1
     imp:n = 1
2002   4   -1.20479E-03   (-2014)
     u=2
     imp:n = 1
2003   4   -1.20479E-03   (2014)
     u=2
     imp:n = 1
c
c
c Imaging Plate
4000   0   (-4000 4001 4002 -4003 4004 -4005)
     imp:n = 1
c
c Volume Above Block Inside End of World Sphere
200   4   -1.20479E-03   (-1 1005)
     imp:n = 1
c
```

```
c Volume Below Block Inside End of World Sphere
201   4   -1.20479E-03   (-1 -4001)
    imp:n = 1
c
c Volume Around BPI Block Z-plane limits
202   4   -1.20479E-03   (-1 1004 -1005)(-1000:1001:-1002:1003)
    imp:n = 1
c
c Volume Gap Between BPI Block and Collimator
203   4   -1.20479E-03   (-1 -1004 2000)
    imp:n = 1
c
c Volume Around Collimator Z-plane limits
204   4   -1.20479E-03   (-1 -2000 2001)(-2002:2003:-2004:2005)
    imp:n = 1
c
c Volume Gap Between Collimator and Imaging Plate
205   4   -1.20479E-03   (-1 -2001 4000)
    imp:n = 1
c
c Volume Around Imaging Plate Z-Plane Limits
206   4   -1.20479E-03   (-1 -4000 4001)(-4002:4003:-4004:4005)
    imp:n = 1
c
c End of World Sphere
1   0   (1)   imp:n = 0
c
c Blank line required here.

c ********** BLOCK 2: SURFACE CARDS **********
c
c BPI Block
1000 PX -1.250
1001 PX  1.250
1002 PY -1.250
1003 PY  1.250
1004 PZ -0.800
1005 PZ  0.000
1006 CZ  0.800
c
c Collimator Block
2000 PZ -0.900
2001 PZ -1.000
2002 PX -1.650
2003 PX  1.650
2004 PY -1.650
2005 PY  1.650
c
```

```
c Collimator Grid
2010 PX  0.0000
2011 PX  0.0010
2012 PY  0.0000
2013 PY  0.0010
2014 C/Z 0.0005 0.0005  0.0004
c
c Test Discs Flush with Front Surface
3010 C/Z -0.85 -0.85  0.2
3011 C/Z  0.85 -0.85  0.2
c Use 1005 for top cutoff
3012 PZ -0.200
c
c Test Discs Flush with Rear Surface
3020 C/Z -0.85  0.85  0.2
3021 C/Z  0.85  0.85  0.2
3022 PZ -0.600
c Use 1004 for bottom cutoff
c
c Test Rod on Front Face
3030 C/X -0.850 -0.035  0.035
3031 PX -0.605
3032 PX  0.595
c
c Test Rod on Rear Face
3040 C/X 0.850 -0.764  0.035
c Use 3031 for lower X plane
c Use 3032 for upper X plane
c
c Imaging Plate
4000 PZ -2.225
4001 PZ -3.225
4002 PX -1.408
4003 PX  1.408
4004 PY -1.408
4005 PY  1.408
c
c End of World Sphere
1 so 550.00
c
c
c Blank line required here.

c ********** BLOCK 3: DATA CARDS ************************************
c
mode n
c
c ********** BLOCK 4: TALLY DEFINITION ******************************
```

```
c
FMESH14:n  Geom = xyz  Origin = -1.408 -1.408 -3.225
          IMESH = 1.408   IINTS = 2048
          JMESH = 1.408   JINTS = 2048
          KMESH = -2.225  KINTS = 1
          OUT = col
c
c ***************** BLOCK 5: SOURCE DEFINITION ******************************
c
SDEF   PAR=1   POS=0.00 0.00 500.00   ERG=d1
     x=d2   y=d3   z=0   VEC=0 0 -1   DIR=1
c
SI1 A  1.08273E-09  1.18659E-09  1.30590E-09  1.39589E-09  1.51081E-09
     1.73337E-09  1.90762E-09  2.01371E-09  2.17957E-09  2.38871E-09
     2.58534E-09  2.80995E-09  2.99104E-09  3.26443E-09  3.44590E-09
     3.77653E-09  4.08750E-09  4.35099E-09  4.70926E-09  5.05476E-09
     5.49380E-09  6.09666E-09  6.46279E-09  6.96590E-09  7.44590E-09
     8.09265E-09  8.79562E-09  9.32374E-09  1.01759E-08  1.08770E-08
     1.17726E-08  1.27421E-08  1.37339E-08  1.51147E-08  1.60223E-08
     1.71264E-08  1.88485E-08  2.01477E-08  2.18979E-08  2.36028E-08
     2.57605E-08  2.77660E-08  2.91893E-08  3.18579E-08  3.49157E-08
     3.71671E-08  4.10756E-08  4.44595E-08  4.97532E-08  5.52152E-08
     5.95162E-08  6.30922E-08  6.88628E-08  7.39187E-08  8.06801E-08
     8.69667E-08  9.29649E-08  1.01469E-07  1.08016E-07  1.18390E-07
     1.26031E-07  1.37561E-07  1.48281E-07  1.58509E-07  1.73009E-07
     1.84175E-07  2.02704E-07  2.19409E-07  2.33566E-07  2.54930E-07
     2.70245E-07  2.96193E-07  3.17940E-07  3.42707E-07  3.70948E-07
     3.94872E-07  4.30991E-07  4.70402E-07  5.04938E-07  5.46542E-07
     5.86671E-07  6.35009E-07  6.90205E-07  7.37809E-07  8.05281E-07
     8.60814E-07  9.31741E-07  1.00852E-06  1.08709E-06  1.17176E-06
     1.26305E-06  1.36713E-06  1.49840E-06  1.58843E-06  1.70504E-06
     1.85324E-06  2.01432E-06  2.19855E-06  2.32099E-06  2.53324E-06
     2.73057E-06  2.93104E-06  3.22587E-06  3.44832E-06  3.71691E-06
     3.94027E-06  4.30066E-06  4.71357E-06  4.99680E-06  5.45378E-06
     5.78151E-06  6.31023E-06  6.83014E-06  7.42385E-06  8.13659E-06
     8.55400E-06  9.33624E-06  1.01477E-05  1.08475E-05  1.17903E-05
     1.26033E-05  1.36987E-05  1.48895E-05  1.60493E-05  1.72996E-05
     1.83391E-05  2.00162E-05  2.16656E-05  2.31595E-05  2.50679E-05
     2.71333E-05  2.94917E-05  3.19217E-05  3.41227E-05  3.69345E-05
     3.96463E-05  4.32722E-05  4.68377E-05  5.02762E-05  5.51032E-05
     5.76887E-05  6.34914E-05  6.92975E-05  7.34616E-05  7.91841E-05
     8.42922E-05  9.31585E-05
c
SP1   2.28437E+05  2.55487E+05  2.57181E+05  2.65790E+05  2.87639E+05
     3.21703E+05  3.39104E+05  3.66976E+05  3.66985E+05  3.85564E+05
     4.26982E+05  4.34076E+05  4.68213E+05  4.87084E+05  5.46549E+05
     5.81827E+05  6.09273E+05  6.35914E+05  6.68105E+05  6.97321E+05
     7.39890E+05  7.82484E+05  7.85077E+05  8.19408E+05  8.49629E+05
```

```
     8.95583E+05  9.34749E+05  9.59700E+05  1.00497E+06  1.06632E+06
     1.12770E+06  1.16545E+06  1.23659E+06  1.28644E+06  1.31644E+06
     1.35158E+06  1.36054E+06  1.35610E+06  1.40150E+06  1.43419E+06
     1.46283E+06  1.51180E+06  1.51681E+06  1.52185E+06  1.51689E+06
     1.51692E+06  1.49221E+06  1.45348E+06  1.40647E+06  1.36547E+06
     1.29974E+06  1.23310E+06  1.14702E+06  1.08108E+06  9.92458E+05
     9.02149E+05  8.28192E+05  7.57804E+05  6.97972E+05  6.20016E+05
     5.56226E+05  4.97363E+05  4.43267E+05  4.04259E+05  3.65064E+05
     3.25357E+05  2.97706E+05  2.75105E+05  2.54220E+05  2.34921E+05
     2.26574E+05  2.12848E+05  1.99952E+05  1.89078E+05  1.75878E+05
     1.72443E+05  1.58307E+05  1.53187E+05  1.44856E+05  1.37883E+05
     1.29104E+05  1.23294E+05  1.15824E+05  1.06329E+05  1.01545E+05
     9.50789E+04  9.05020E+04  8.44613E+04  7.93442E+04  7.60233E+04
     7.09490E+04  6.64315E+04  6.22021E+04  5.90129E+04  5.67293E+04
     5.29429E+04  5.02288E+04  4.68764E+04  4.34602E+04  4.16415E+04
     3.96368E+04  3.74812E+04  3.52106E+04  3.32957E+04  3.19021E+04
     2.97725E+04  2.76941E+04  2.62745E+04  2.46825E+04  2.34173E+04
     2.18541E+04  2.08707E+04  1.99972E+04  1.86626E+04  1.77641E+04
     1.64695E+04  1.58324E+04  1.49222E+04  1.40642E+04  1.32558E+04
     1.26592E+04  1.20499E+04  1.11351E+04  1.06340E+04  1.00227E+04
     9.44642E+03  8.96218E+03  8.44697E+03  8.04031E+03  7.52838E+03
     7.18961E+03  6.82104E+03  6.45010E+03  6.15982E+03  5.80570E+03
     5.45395E+03  5.14044E+03  4.86088E+03  4.65744E+03  4.40418E+03
     4.16462E+03  3.93816E+03  3.77336E+03  3.54472E+03  3.36299E+03
     3.19058E+03  2.99731E+03
c
SI2    -3.00   3.00
SP2     0      1
SI3    -3.00   3.00
SP3     0      1
c
c ***************** BLOCK 6: MATERIAL DEFINITION ****************************
c
c Material 1 is min40%Boron Nitride
c Material 1 density is: 2.100 [g/cm^3]
M1   5010 -0.0796   5011 -0.3204
     7014 -0.597792   7015 -0.002208
c
c Material 2 is Teflon (Polytetrafluoroethylene)
c Material 2 density is: 2.200 [g/cm^3]
M2   6012 -0.2376130419   6013 -0.0025699581
     9019 -0.759817
c
c Material 3 is Collimator 10% Nat-Gd, 6.8% B-10, 83.2% SiO2
c Material 3 density is: 2.650 [g/cm^3]
M3   64000 -0.1000
     5010 -0.0680
     14000 -0.38891
```

```
     8016 -0.44309
c
c Material 4 is air
c Material 4 density is: 1.20479E-03 [g/cm^3]
M4   6012 -0.0001226732    6013 -0.0000013268
     7014 -0.75248761744   7015 -0.00277938256
     8016 -0.231781
     18000 -0.012828
     GAS=1
c
c Material 6 is Cd
c Material 6 density is: 8.650 [g/cm^3]
M6   48000 1
c
c Material 7 is Pb
c Material 7 density is: 11.35 [g/cm^3]
M7   82000 1
c
c ***************** Energy, Time, and Weight Cutoff *************************
c
c The CUT command specifies the minimum energy, time, or particle weight below
c which the particle is killed.
c Neutrons with energy below 1.00E-10 MeV are killed.
c "1j" jumps over "1" input parameter and uses the default value for the jumped
c paramater (the "time cutoff" in this case).
c
cut:n  1j  1.00E-10
c
c ***************** Physics Simplification *********************************
c
c ***************** NUMBER OF PARTICLE HISTORIES ***************************
nps 1E11
```

References

[0] Barton, J P. SOME POSSIBILITIES OF NEUTRON RADIOGRAPHY. p., 1964. Web. doi:10.1088/0031-9155/9/1/303.

[1] Proceedings of the American Philosophical Society, Vol. 152, No. 3 (Sep., 2008), pp.349-361

[2] Panchbhai AS. Wilhelm Conrad Röntgen and the discovery of X-rays: Revisited after centennial. J Indian Acad Oral Med Radiol 2015;27:90-5

[3]Howell, Joel D. "EARLY CLINICAL USE OF THE X-RAY" Transactions of the American Clinical and Climatological Association vol. 127 (2016): 341-349.

[4] Petrik, Vladimir, Apok, Vinothini, Britton, Juliet A., Bell, B Anthony, Papadopoulos, Marios C.. Godfrey Hounsfield and the Dawn of Computed Tomography. (2006) Neurosurgery. 58 (4): 780. doi:10.1227/01.NEU.0000204309.91666.06 - Pubmed

[5] https://www.nobelprize.org/prizes/medicine/2003/lauterbur/biographical/

[6] amadian R, Goldsmith M, Minkoff L. NMR in cancer: XVI. FONAR image of the live human body. Physiol Chem & Phys 1977; 9:97-109.

[7] Nelson, R.O.; Vogel, S.C.; Hunter, J.F.; Watkins, E.B.; Losko, A.S.; Tremsin, A.S.; Borges, et al. Neutron Imaging at LANSCE—From Cold to Ultrafast. J. Imaging 2018, 4, 45.

[8] John R. White AJaJB. Preliminary characterization of the irradiation facilities within the LEU-Fueled Umass-Lowell Research Reactor. PHYSOR. May 7-11, 2000 2000.

[9] Mocko, M.; Muhrer, G.; Tovesson, F. Advantages and limitations of nuclear physics experiments at an ISIS-class spallation neutron source. Nucl. Instrum. Methods Phys. Res. 2008, 589, 455–464.

[10] Ino, T.; Ooi, M.; Kiyanagi, Y.; Kasugai, Y.; Maekawa, F.; Takada, H.; Muhrer, G.; Pitcher, E.J.; Russell, G.J. Measurement of neutron beam characteristics at the Manuel Lujan Jr. neutron scattering center. Nucl. Instrum. Methods Phys. Res. 2004, 525, 496–510.

[11] https://www.psi.ch/niag/neutron-imaging-detectors

[12] http://www.rctritec.com/en/scintillators/introduction.html

[13] N. Kardjilov, et al. "A highly adaptive detector system for high resolution neutron imaging." Nuclear Instruments and Methods in Physics Research Section A 651.1 (2011): 95-99.

[14] Siegmund, O.H.; Vallerga, J.V.; Tremsin, A.S.; Feller, W.B. High spatial and temporal resolution neutron imaging with microchannel plate detectors. IEEE Trans. Nucl. Sci. 2009, 56, 1203–1209.

[15] Tremsin, A.S. High resolution neutron counting detectors with microchannel plates and their applications in neutron radiography, diffraction and resonance absorption imaging. Neutron News 2012, 23, 35–38.

[16] Tremsin, A.S.; McPhate, J.B.; Vallerga, J.V.; Siegmund, O.H.; Feller, W.B.; Lehmann, E.; Dawson, M. Improved efficiency of high resolution thermal and cold neutron imaging. *Nucl. Instrum. Methods Phys. Res.* **2011**, *628*, 415–418.

[17] Jenkins, Edward B.Photon counting image sensor development for astronomical applications; NASA STI/Recon Technical Report N; 1987;14049; https://ui.adsabs.harvard.edu/abs/1987STIN...8814049J

[18] Tremsin, A.S.; McPhate, J.B.; Vallerga, J.V.; Siegmund, O.H.; Feller, W.B.; Lehmann, E.; Kaestner, A.; Boillat, P.; Panzner, T.; Filges, U. Neutron radiography with sub-15 μm resolution through event centroiding. Nucl. Instrum. Methods Phys. Res. 2012, 688, 32–40.

[19] Grünzweig, C.; Frei, G.; Lehmann, E.; Kühne, G.; David, C. Highly absorbing gadolinium test device to characterize the performance of neutron imaging detector systems. Rev. Sci. Instrum. 2007, 78, 053708.

[20] Kaestner, A.P.; Kis, Z.; Radebe, M.J.; Mannes, D.; Hovind, J.; Grünzweig, C.; Kardjilov, N.; Lehmann, E.H. Samples to Determine the Resolution of Neutron Radiography and Tomography. Phys. Procedia 2017, 88, 258–265.

[21] Hendrick, R.E.; Raff, U.; Stark, D.D.; Bradley, W.G. Magnetic Resonance Imaging, 2nd ed.; St. Louis: Hong Kong, China, 1992; pp. 109–144.

[22] Nray Services Inc. 56A Head Street Dundas Ontario; Nray Services Inc.: Dundas, ON, Canada.

[23] Neitzel, U.; Egbert, B.; Gerhard, H.; Paul, R. Determination of the modulation transfer function using the edge method: Influence of scattered radiation. Med. Phys. 2004, 31, 3485–3491.

[25] Lin, Eugene, and Adam Alessio. "What are the basic concepts of temporal, contrast, and spatial resolution in cardiac CT?." *Journal of cardiovascular computed tomography* vol. 3,6 (2009): 403-8. doi:10.1016/j.jcct.2009.07.003

[26] Huda, Walter & Abrahams, R. (2015). X-Ray-Based Medical Imaging and Resolution. AJR. American journal of roentgenology. 204. W393-W397. 10.2214/AJR.14.13126.

[27]https://www.nuclear-power.net/nuclear-power/reactor-physics/atomic-nuclear-physics/fundamental-particles/neutron/neutron-energy/

[28] Trtik, Pavel, et al. "PSI 'Neutron Microscope'at ILL-D50 Beamline-First Results." Neutron Radiography: WCNR-11 15 (2020): 23.

[29] Corba M., Ninkov Z. (1995) Modular architecture for real-time astronomical image processing with FPGA. In: Moore W., Luk W. (eds) Field-Programmable Logic and Applications. FPL 1995. Lecture Notes in Computer Science, vol 975. Springer, Berlin, Heidelberg

[30] Mohammad Vali Arbabmir, Seyyed Mohammad Mohammadi, Sadegh Salahshour, and Farshad Somayehee, "Improving night sky star image processing algorithm for star sensors," J. Opt. Soc. Am. A 31, 794-801 (2014)